# Preparation and characterisation of an array of trapped single neutral $^{87}Rb$ atoms for quantum computation and quantum simulation

**A Thesis**

submitted to

Indian Institute of Science Education and Research Pune

in partial fulfillment of the requirements for the BS-MS Dual Degree Programme

by

**Abhishek Ranjith**


Indian Institute of Science Education and Research Pune

Dr. Homi Bhabha Road,

Pashan, Pune 411008, INDIA.

April, 2026

Supervisor: Prof. Dr. Umakant D. Rapol

© Abhishek Ranjith

All rights reserved

# Certificate

This is to certify that this dissertation entitled **"Preparation and characterisation of an array of trapped single neutral $^{87}Rb$ atoms for quantum computation and quantum simulation"** towards the partial fulfilment of the BS-MS dual degree programme at the Indian Institute of Science Education and Research, Pune represents study/work carried out by **Abhishek Ranjith** at Indian Institute of Science Education and Research under the supervision of **Prof. Dr. Umakant D. Rapol**, Professor, Department of Physics, during the academic year 2025 - 2026.

Prof. Dr. Umakant D. Rapol

**Committee:**

Prof. Dr. Umakant D. Rapol

Prof. Dr. Vijayakumar Chikkadi

Dedicated to *Amma, Acha and Anu*

# Declaration

I hereby declare that the matter embodied in the report entitled **"Preparation and characterisation of an array of trapped single neutral $^{87}Rb$ atoms for quantum computation and quantum simulation"** are the results of the work carried out by me at the Department of Physics, Indian Institute of Science Education & Research (IISER) Pune, under the supervision of **Prof. Dr. Umakant D. Rapol**, and the same has not been submitted elsewhere for any other degree.

Wherever others contribute, every effort is made to indicate this clearly, with due reference to the literature and acknowledgement of collaborative research and discussions.

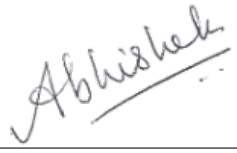

Abhishek Ranjith
20211204

# Acknowledgements

My introduction to the field of cold atoms and related quantum technologies when I first visited the APQO Lab about one and half years ago, was a period of utter bewilderment and enthusiasm, which I will forever remember fondly. This year-long MS thesis project is the first of many more years of passionate science and discoveries, both scientific and personal.

I want to express my immense gratitude to my supervisor, Prof. Dr. Umakant D. Rapol, who paved the way for this amazing journey at a critical junction of my life. His unadultered enthusiasm for experimental physics and active participation in our labs, as well as the cut-to-the-chase interactions/ conversations I had with him has greatly shaped the way I view science, in particular experimental physics. I thank him for entrusting to me such a challenging yet insightful project, which I am lucky to have been a part of. I also thank my expert, Prof. Dr. Vijayakumar Chikkadi, for his kind insights and discussions in the initial phase of this project.

I want to also express my sincere gratitude to my dear lab members, who were also my guiding lights throughout this project – Joel Sunil and Monu Bhartiya – for their constant support, scientific insights, and helping me gradually warmup to the intricacies of the Rb BEC setup. Both of them truly engraved in me the tenacity and the critical thinking which has utmost importance in such a field, as a consequence of our countless brainstorming and reiterations, despite shortcomings, in the development of the tweezers. I also thank my lab-mates and fellow batch-mates – Sharan, Gautam, and Dipansh for their timely help at various points in the project, and more importantly, our friendship! I also extend gratitude to the technical assistance teams and helper staff, especially Mr. Karthikeyan.

Though words will not suffice, I wish to thank my Mom (Mrs. Parvathi Ranjith), Dad (Mr. Ranjith Raman) and Sis (Ms. Anagha Ranjith) for their constant background support in all forms, and I dedicate this thesis to them! Special thanks to my roommate – Anuvind – for being there for me always. Last, but not the least, I extend my heartfelt gratitude to my friends who are no less than family – Aratrik, Sumit and Aswin – for the wonderful memories created on and off the volleyball court.

# Abstract

This thesis investigates the experimental realization and characterization of single neutral $^{87}Rb$ atoms trapped in optical tweezer arrays, a critical step toward developing scalable quantum processors with long coherence times.

An Acousto-Optic Deflector (AOD) conjugated to a high-NA microscope objective generates multiple diffraction-limited spots from the 813 nm trapping laser. These tweezers are loaded from the centre of a Magneto-Optical Trap (MOT) cloud. A primary focus of this thesis is the light-assisted collisions mechanism, which is responsible in reducing the trap occupation numbers to sub-Poissonian values via pairwise/ singular trap losses. Hence, the cooling 780 nm laser is used for both fluorescence imaging as well as inducing these inelastic collisions. Theoretically, operating in the "collisional blockade regime" should limit trap occupancy to a single atom by ensuring trap loss rates dominate loading rates. Experimental characterization of atom occupation trends involved both red- and blue-detuned collision beams. Results indicated a beam waist of 1.83 $\mu$m which exceeds the sub-micron threshold required for a robust collisional blockade. Consequently, the fluorescence histograms revealed multi-modal signatures (0 to 3 atoms) rather than the ideal bimodal (0 or 1) occupancy. However, a significant reduction in mean occupation at higher detunings confirmed the effectiveness of the collision mechanism in achieving sub-Poissonian statistics. The work further details the design of a miniaturized, portable science chamber intended for field-deployed quantum computing. While the initial vacuum bake-out failed to reach Ultra-High Vacuum (UHV) due to epoxy cracking in the custom cell, the design remains a viable prototype for future iterations. Furthermore, the temporal responsivity of an AOM was investigated for possible generation of time-shared arrays of trapped single atoms.

This work successfully demonstrates the generation of a 1D array of trapped atoms with multimodal occupations, and provides a comprehensive analysis of loading dynamics and hardware constraints. The findings emphasize that AOD operational wavelengths, objective numerical aperture, and imaging losses are critical factors in perfecting scalable neutral-atom qubit arrays.

# Contents

# List of Figures

# List of Tables

# Chapter 1

# Introduction

The paradigm shift from Classical Physics in the last century, namely Quantum Mechanics, allows a thorough description of the physical phenomena at the atomic scale, or at the so-called quantum level. The necessity to depart from classical mechanics arose from the experimental results concerning the radiation spectra of black bodies, the famous photoelectric effect, as well as the Davisson-Germer electron diffraction experiment displaying the wave-particle duality of light and matter, and the explanation for the stability of the atomic energy levels. The introduction of revolutionary ideas such as discretisation/quantization and the superposition principle were the keystone features of the quantum mechanical formulation [1].

Since the inception and development of quantum mechanics, there has been a growing need for precise simulation of quantum-mechanical systems (such as atoms, molecules, solid-state systems, tunneling junctions, etc.) to understand their behaviour better and to utilize their exotic properties for quantum technologies. As the atomic number goes up, as the molecules become larger with greater numbers of atomic species, or as the size of the solid-state system scales up, the problem of simulation gets exponentially more complex and time-consuming for classical computers. The Nobel laureate and physicist Richard Feynman, in May 1981, proposed his vision of using a toy model made up of quantum-mechanical systems themselves (quantum computers) to simulate other quantum-mechanical systems (or Nature herself!!) [2]. The field of quantum computing revolutionized computation by harnessing the principles of quantum mechanics - Qubits (aka quantum bits), unlike classical bits, can exist in a superposition of states and exhibit entanglement. These properties enable quantum parallelism, offering exponential speed-ups in solving certain classes of problems algorithmically that are intractable for classical computers. The applications of quantum computers span drug discovery, materials science modeling, optimization problems, financial modeling, and secure communication.

To build a functional quantum computer, the host physical system must satisfy a set of stringent requirements known as Di-Vincenzo's criteria. A plethora of physical systems have been identified that can serve as a suitable platform to carry out quantum computation, the most notable ones being trapped ions, trapped neutral atoms, transmon/flux-based superconducting circuits, NV centers, NMR spin states, quantum dots, and single photons. Among the various platforms being explored, trapped neutral atom arrays have emerged as a promising candidate, demonstrating high scalability and connectivity, as well as long coherence times and intermediate computational speeds, enabling a comparable quantum volume to that of ion traps.

## 1.1 Di-Vincenzo's Criteria and Trapped Neutral Atoms

Proposed by the physicist David Di-Vincenzo in 2000 [3], Di-Vincenzo's criteria constitute essential prerequisites that every physical system must fulfill to qualify as a functional quantum computer. In this section, I will highlight the suitable features of trapped neutral atoms, specifically of an isotope of Rubidium, $^{87}Rb$, that make them an ideal platform for quantum computers. The five criteria are as follows:

### 1. A scalable physical system made up of well-characterized Qubits:

A well-characterized Qubit is one which has a precisely defined two-level system, capable of having fast and high-fidelity transitions between the two states. $^{87}Rb$ has been thoroughly investigated spectroscopically for its energy levels for a very long time. The $D_1$ (795 nm) and $D_2$ (780 nm) transitions that enable laser cooling and imaging of $^{87}Rb$ have been extensively documented [4]. Moreover, the development of the 780 nm lasers based on Ti: Sapphire and $AlGaAs$ allowed extensive usage of $^{87}Rb$ as an ideal candidate for quantum simulators, atom optics, and ultra-cold atoms experiments for about three decades. More about the cooling, trapping, and imaging schemes will be revisited later in Chapter 2. The Qubit is, however, realized using the two hyperfine levels of the ground state $5^2S_{1/2} : F = 1$ and $F = 2$. These hyperfine levels are split by a microwave frequency of about 6.8 GHz, as will be shown later in this section.

Quantum advantage refers to the super-polynomial speedup in solving certain tasks (regardless of whether it is useful or not) conferred by quantum computational algorithms that the best possible classical computational algorithms simply cannot solve in a feasible amount of time [5]. A scalable system is crucial to the physical realization of quantum advantage or quantum supremacy. The advent of technologies such as Spatial Light Modulators (SLM), Digital Micro-mirror Devices (DMD), along with assisting technologies such as Acousto-Optic Deflectors (AOD), makes it possible to generate up to a million spatially reconfigurable optical tweezers, making it possible to

scale up the number of logical Qubits easily in the case of trapped neutral atoms. The theory and demonstration of the experimental setup utilizing these devices for array generation will be given in Chapters 2 and 3 respectively.

## 2. The ability to initialize the state of the Qubits to a simple fiducial state:

The initialization of all Qubits to a simple fiducial state allows a deterministic start to any quantum algorithm. In the case of $^{87}Rb$, global illumination with optical pumping light to pump all atoms into some dark state is a widely used strategy. For example, $\sigma_-$ polarized cooling and repumper light ($D_2$ line) can be used to continuously push all $^{87}Rb$ atoms into the only dark state, $5^2S_{1/2}, F = 2, m_F = -2$ for Rydberg protocols. Alternatively, $\pi$ polarized Raman two-photon transitions can be used to de-pump atoms continuously into the only dark state $5^2S_{1/2}, F = 1, m_F = 0$, due to the forbidden transition $\Delta F = 0, m_F = 0, m_{F'} = 0$. The above strategies are visualized in Fig.1.1(a) and 1.1(b), adapted from [6].

## 3. Long relevant quantum coherence times:

The duration for which a qubit retains its state information before it decoheres due to environmental factors is called the quantum coherence time. There are two important timescales that experimentalists concern themselves with to determine the different kinds of decohering times: $T_1$ measures the longitudinal/amplitude relaxation, i.e., the relaxation of the excited state $|1\rangle$ to the ground state $|0\rangle$; $T_2$ measures the transverse relaxation/dephasing, i.e., loss of phase information. In general, $T_2 < 2\,T_1$. Trapped single neutral $^{87}Rb$ atoms display $T_1$ times upto a few seconds whilst having $T_2$ times of the order of hundreds of milliseconds. With a relatively fast gate implementation of a few microseconds and present advances surpassing the 4 9's (i.e. 99.99 %) in terms of fidelity, this platform promises a large quantum volume almost on par with trapped ions- and superconducting circuit-based Qubits [6, 7]. An added feature available with trapped atoms is their really long trap lifetimes, lasting up to a few seconds, making it possible for entire quantum algorithms to be fully executed before collision/scattering-induced atom losses from the tweezers.

## 4. A universal set of quantum gates to perform any quantum computation:

Two possible schemes for one-qubit rotation gates exist, allowing state manipulation: using Microwave + RF pulses to directly excite the $F = 1$ state to the $F = 2$ state; or using a two-photon Raman transition (possibly using lasers red-detuned to either of the D line transitions). On the other hand, multi-qubit entangling gates are realized using two-photon transitions to highly excited Rydberg states (i.e., $n \sim 70$), which enable physical entanglement amongst neighbouring atomic

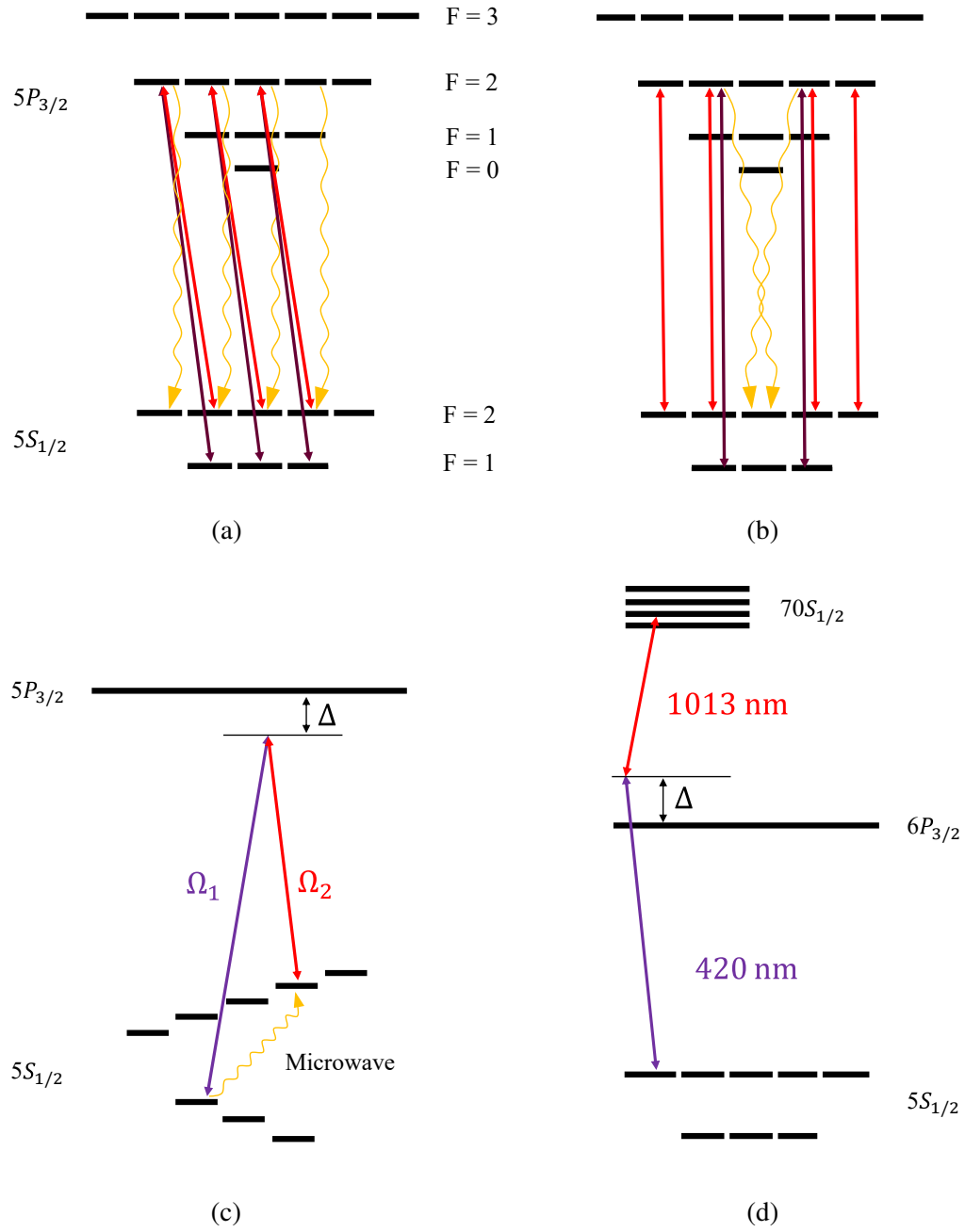


Figure 1.1: (a) Optical pumping using $\sigma_-$ polarized light and repumper; (b) Optical pumping using $\pi$ polarized light and repumper; (c) One-Qubit gate using a $\sigma_+$ polarized 2-photon Raman transition or Microwave pulse; (d) 2-photon $m_F$-preserving excitation to Rydberg state.

sites via the phenomenon of Rydberg Blockade. The principle of this mechanism is that two atoms within the Rydberg blockading radius (up to $R_b \sim 10\ \mu$m) cannot be simultaneously excited to a Rydberg state due to the repulsive dipole-dipole interaction at short distances owing to their large size (hence their large polarizability). The level diagrams for these gate implementations are shown in Fig.1.1(c) and 1.1(d), again adapted from [6].

### 5. A Qubit-specific readout measurement capability:

Qubit measurement modality is paramount to quantum information and computation, as it allows the readout of the solution of a quantum algorithm/protocol. For hyperfine or Rydberg Qubits of $^{87}Rb$, an optical push-out scheme is utilized in both cases. In case of hyperfine state readout, the ground state is dark to the push-out pulse driving $F = 2 \longrightarrow F' = 3$. Thus, atoms in the excited state are heated out, leaving behind empty tweezers, while ground state atoms are imaged in the following sequence. Similarly, in the case of Rydberg state detection, the tweezers are momentarily switched off while pulsing the Rydberg lasers, and the anti-potential offered by the tweezers kicks out the Rydberg atoms ($|r\rangle$) whilst retaining the ground state atoms ($|g\rangle$). Subsequent fluorescence imaging can be interpreted as a binary readout, where empty traps = 1 and occupied traps = 0.

With this, the favourable properties and technologies that enable trapped neutral atoms to emerge as a promising candidate platform for scalable quantum computers have been sequentially enunciated. In the next section, some light on the advent and importance of optical tweezers will be shed, which enable us to capture and manipulate these natural Qubits in the first place!

## 1.2 History of Optical Tweezers

Rather than a solitary spark of genius, purely optical confinement of single atoms (aka optical tweezers!) materialized as a consequence of a series of ideas, theories, innovations, and experiments spanning many decades, as I will briefly recount here.

The notion that light could exert a physical force on matter is centuries old. In the early $17^{th}$ century, Johannes Kepler observed that the tails of comets always pointed away from the sun, hypothesizing that a solar pressure could be responsible for blowing the material outward. A rigorous theoretical framework emerged with the Maxwellian unification of electricity and magnetism in the $19^{th}$ century. It was shown that the electromagnetic field carries momentum, angular momentum, as well as propagates energy. Light reflecting off of or absorbed by a surface, transfers a finite amount of momentum to that object, applying radiation pressure. The magnitude of this force is immeasurably small in everyday contexts, and it remained utterly difficult to isolate from other

radiometric forces. With the invention of the laser in 1960, the availability of a coherent, intense, and collimated beam of light finally granted experimentalists the power to observe and harness radiation pressure to manipulate matter physically.

Arthur Ashkin, while studying the effects of laser light on micron-sized, transparent, dielectric particles, observed two distinct forces at play: a scattering force that pushes the particle in the direction of light propagation, arising from the momentum transfer of scattered photons, aka radiation pressure, and the gradient force that pulls the particle toward the region of light intensity maxima, which is conservative in nature. In 1970, Ashkin demonstrated the first stable optical trap using two opposing laser beams to balance the scattering forces axially, while relying on the gradient force to confine the particles azimuthally [8]. In 1986, the single-beam gradient force trap, or the optical tweezer, was demonstrated by focusing a laser beam extremely tightly through a high-numerical-aperture objective, earning him a Nobel Prize in Physics in 2018 [9]. The axial gradient force became strong enough to overcome the scattering forces, essentially creating a 3D potential well where small dielectric particles could be stably held in free space.

Initially applied to biological samples, a theoretical curiosity about extending the principles to even smaller dielectric particles, namely polarizable atoms themselves, opened the path to trapping ultra-cold atoms. Atoms are about tens of billions of times lighter but polarizable spheres that interact with light primarily through resonant absorption and emission, complicating trapping due to heating. Trapping atoms purely using light was possible after the discovery of laser cooling (e.g., Doppler cooling and Magneto-Optical Trap (MOT)), which could slow atoms from hundreds of meters per second to centimeters per second. Sufficiently cold atoms could then be subjected to an optical potential well arising from gradient forces, leading to the first Optical Dipole Traps (ODT) [10, 11]. The same gradient force used for dielectric micro-spheres could trap atoms via the AC Stark shift, completely isolated from the thermal environment outside the vacuum chamber walls. I will further discuss the working principle, theory, and generation of multiple such ODTs in Chapter 2.

Today, the optical tweezer has evolved from a tool for trapping single particles into a scalable architecture for quantum information processing. In modern neutral atom platforms, highly focused laser beams are used to trap individual atoms ( $^{87}Rb$, $^{87}Sr$, $^{171}Ybb$) in 2-D/3-D arrays. The salient features offered by the usage of optical tweezers are as follows:

**Scalability:** By using diffractive optical elements or spatial light modulators, a single laser source can be split into hundreds or thousands of tweezers, each holding a single atom.
**Control:** Unlike ions, neutral atoms do not repel each other via Coulomb forces, allowing them to be packed tightly (within micrometers) without instability.

**Connectivity:** With the use of Acousto-Optic Deflectors, the trapped atoms can be moved around, and multi-qubit entangling gates are easily realized with a high degree of connectivity.

Henceforth in this thesis, Optical Dipole traps (ODT) will be interchangeably referred to as optical tweezers or far-off-resonant traps (FORTs) or merely just as traps.

## 1.3 Aim and Scope of the Project

The motivation for this project is to demonstrate the first criterion outlined in Section 1.1 for a neutral atoms platform by utilizing existing architecture built originally for $^{87}Rb$ BEC/ atom optics experiments. The primary objective is to experimentally realize and characterize an array of trapped single neutral $^{87}Rb$ atoms. A secondary objective is to demonstrate miniaturization of this system for portable deployment, using a miniature MOT setup which has been successfully demonstrated in our lab previously [12].

In particular, this project involves developing and characterizing the necessary hardware and techniques for generating and loading the trapped atom arrays that form the qubit register, while employing a wide range of expertise, from optics and electronics to programming and engineering. This project also directly aligns with the efforts of the National Quantum Mission to develop scalable quantum computers capable of demonstrating a clear quantum advantage within the country.

## 1.4 Overview of the Thesis

This thesis is divided into 5 chapters, which will sequentially guide the reader through the tweezer generation, loading and characterization of the trapped atom arrays. The structuring is as follows:

**Chapter 2:** In this chapter, some insights from a literature survey will be produced, and the theory behind the various stages involved in the trapping of atoms will be explained.

**Chapter 3:** In this chapter, the experimental setup of the tweezers will be provided. Additionally, a section will display the setup for a miniature version for demonstrating trapped single neutral atoms.

**Chapter 4:** Here, the experimental methodology of data acquisition and analysis techniques will be explained and the results obtained therein will be shown. These include pre-requisite trap characterisations, background device calibrations used in the generation of the arrays, measurement of trap frequencies and depth, loading trends of atoms in the tweezers, single-atom detection

through controlled loading, and the vacuum bake-out results. The setbacks and challenges faced experimentally in the realization of every result are also shared.

**Chapter 5:** In this discussion, the results in the previous chapter will be summarised and interpreted, along with the concluding remarks about this project. A brief outline of the future outlook and the promises that this project holds will also be shared.

# Chapter 2

# Theoretical Background

This Chapter is divided into three parts: Literature review, Theory and a section on $^{87}Rb$. We will begin with a brief literature review outlining key advancements in loading, array generation, reconfiguration, and imaging in optical trapping of neutral $^{87}Rb$ atoms.

## 2.1 Literature Review

The fundamental challenge encountered while loading atoms into tweezers is the collisional blockade mechanism. It serves as a boon as well as a bane in experimentally observing singly trapped atoms. When multiple atoms enter a tightly focused trap, light-assisted collisions cause rapid pairwise loss, resulting in a single atom but with a maximum probability of 50 % [13]. To overcome this stochastic limit, experimental groups have divulged into two main strategies. The first involves enhanced loading protocols, such as the use of blue-detuned light-assisted collisions and hyperfine-state-specific laser light. This can push loading probabilities up to 80 % – 90 % by precisely engineering the collisional loss channels and molecular potentials [14]. The second and more dominant strategy accepts the 50 % limit as an initial condition and uses active spatial tweezer reconfiguration to build defect-free deterministic arrays, effectively shifting the burden from physics to algorithmic control [15].

The generation of large-scale trap arrays has evolved significantly, with two diffractive optical technologies being front-runners in this pursuit: Phase-only Spatial Light Modulators (SLMs) and Acousto-Optic Deflectors (AODs). The use of SLMs to create static, arbitrary 2D geometries consisting of hundreds of traps with real-time feedback on trap parameters is a fairly common practice in the recent past [16]. SLMs offer high power efficiency and stability but suffer from slow refresh rates, making them unsuitable for real-time atom transport. On the other hand, AODs

enable rapid steering of laser beams and are used to generate dynamic, reconfigurable arrays, where trap positions can be updated in microseconds. Current state-of-the-art GPUs often combine both of these. An SLM generates a large static registry of traps, while moving AOD tweezers pick and drop atoms to create a defect-free lattice [6]. The ability to rearrange atoms into defect-free clusters as well as to provide all-to-all connectivity for performing multi-qubit gates is arguably the defining advantage of neutral atom platforms over any other rigid architectures such as superconducting qubits, NMR spin qubits, topological qubits etc.

The algorithms used to rearrange the atoms have also progressed in terms of optimisation of number of moves, distance travelled, atom losses, time required etc. The criticality of the algorithm becomes more evident as the array sizes increase. Algorithms with differing strategies based on the system parameters, such as Heuristic Cluster Algorithm (least number of moves), Heuristic Path-Finding Algorithm (shortest path), Hungarian Algorithm (least time), and A Searching Algorithm (collision avoidance), provide superior speedups/improvements in the reconfiguration task according to the necessity of the quantum protocol ahead.

High-fidelity state detection is essential for quantum error correction. The standard method involves collecting scattered fluorescence photons from the cooling probe light through an EMCCD. While this method is effective, it is temporally limited by the long exposure times ($10-50$ ms), numerically limited by small collection efficiency ($1\ \% - 5\ \%$) and often results in atom loss (destructive read-out). Non-destructive readout strategies, such as photon-count-triggered shuttering of probe light to prevent excessive heating, the use of an SPD fibre/qCMOS camera, etc., enable mid-circuit measurements without the need for long reloading of empty traps [17, 18]. More recently, integrating optical cavities with tweezer arrays has proppelled the collection efficiencies of scattered photons close to one.

Hence, we have reviewed how smart classical engineering has helped to tame the complex quantum problems posed by the nature of the neutral-atom platform. Next, let us delve into the theory involved in the various stages of trapping neutral atoms.

## 2.2 Theory

### 2.2.1 Optical Dipole Traps

As seen for dielectric microspheres, there exist gradient and scattering forces for neutral atoms as well, with the same general properties. The scattering forces arise out of the resonant absorption and emission of light, and impart momentum in the direction of propagation of the light. The gradient force arises out of the interaction of the induced electric dipole moment of the polarizable

atom with the intensity gradient of the laser field, and generates a conservative field. The trapping principle in case of neutral $^{87}Rb$ atoms depends on the attractive optical potential well generated by the AC Stark effect of a far-detuned tightly focused laser beam. As a starting point, the theory can be derived semi-classically by considering the neutral atom to be a two-level system and considering the valence electron as a simple classical harmonic oscillator in a classical driving light field [11]. Let the linearly polarized complex driving electric field of the laser light be $\vec{E}(\vec{r},t) = \hat{x}\, E(\vec{r})e^{-i\omega t} + c.c.$, where $\omega$ is the driving optical frequency. The instantaneous induced complex dipole moment of an atom located at $\vec{r}$ is synchronized with the driving field, $\vec{\mu}(\vec{r},t) = \hat{x}\ \mu(\vec{r})e^{-i\omega t} + c.c.$. The dipole moment amplitude is connected to the driving field amplitude via $\mu(\vec{r}) = \alpha(\omega)E(\vec{r})$, where $\alpha(\omega)$ is the complex, frequency-dependent polarizability of the atom. Then, the potential energy is obtained simply as,

$$U_{dip}(\vec{r}) = -\frac{1}{2}\langle\vec{\mu}(\vec{r},t)\cdot\vec{E}(\vec{r},t)\rangle = -\frac{1}{2\epsilon_0 c}Re(\alpha)I(\vec{r}) \tag{2.1}$$

Here, $I(\vec{r}) = 2\epsilon_0 c|E(\vec{r})|^2$ is the intensity of the field, with $\epsilon_0$ and $c$ being the vacuum permittivity and speed of light in free space respectively. Hence, the conservative gradient force naturally arises as a consequence of the gradient of the spatial intensity profile of the light beam, whose nature we will deduce later in this sub-section. The power absorbed by the oscillating dipole is derived as $\langle\dot{\vec{\mu}}(\vec{r},t)\cdot\vec{E}(\vec{r},t)\rangle$. Viewing the laser beam as a stream of photons enables the calculation of the scattering rate of the atom as,

$$\Gamma_{scat}(\vec{r}) = \frac{1}{\hbar\omega}\langle\dot{\vec{\mu}}(\vec{r},t)\cdot\vec{E}(\vec{r},t)\rangle = \frac{1}{\hbar\epsilon_0 c}Im(\alpha)I(\vec{r}) \tag{2.2}$$

The scattering force is directly given by the product of the momentum kick per absorption and the scattering rate. As we can see, determining the complex polarizability $\alpha(\omega)$ directly gives us the gradient and scattering forces, in terms of the laser beam parameters. We can classically obtain the differential equation of motion for the valence electron $-e$ bound elastically to the atomic kernel in the driving field as $\ddot{x}(t) + \Gamma_\omega\dot{x}(t) + \omega_0^2 x(t) = -\frac{-eE(t)}{m}$ , where $\Gamma_\omega = \frac{e^2\omega^2}{6\pi\omega_0 mc^3}$ is the damping rate as described by the Larmor formula for power radiated by accelerated charges, $\omega_0$ is the angular optical transition/ natural frequency between the two levels, and $m$ is the electronic mass. Relating the dipole moment amplitude to the position as $\mu(t) = -ex(t) = \alpha(\omega)E(t)$, we solve for the complex polarizability to get,

$$\alpha(\omega) = \frac{e^2}{m}\frac{1}{\omega_0^2 - \omega^2 - i\omega\Gamma_\omega} \tag{2.3}$$

An important subtlety to note here is that the classical result Eq.(2.3) is valid approximately only when the transition is far from saturation, and we will see shortly that the trapping light barely saturates as we are only interested in the far-detuned case. Substituting the natural line-width of the transition, $\Gamma = (\omega_0^2/\omega^2)\Gamma_\omega$ and Eq.(2.3) into Eq.(2.1) and Eq.(2.2) gives us:

$$U_{dip}(\vec{r}) = -\frac{3\pi c^2}{2\omega_0^3}\left(\frac{\Gamma}{\omega_0 - \omega} + \frac{\Gamma}{\omega_0 + \omega}\right) I(\vec{r}) \tag{2.4}$$

$$\Gamma_{scat}(\vec{r}) = \frac{3\pi c^2}{2\hbar\omega_0^3}\left(\frac{\omega}{\omega_0}\right)^3 \left(\frac{\Gamma}{\omega_0 - \omega} + \frac{\Gamma}{\omega_0 + \omega}\right)^2 I(\vec{r}) \tag{2.5}$$

For trapping experiments, the detuning $\Delta = \omega - \omega_0$ is much smaller compared to the optical transition frequency. Thus, the contribution of the second resonance term in both Eq.(2.4) and Eq.(2.5) can be neglected in the rotating wave approximation ($|\Delta| \ll \omega_0$ & $\frac{\omega}{\omega_0} \approx 1$). Thus, the equations reduce to simple dependencies on the detuning and intensity of the trapping light

$$U_{dip}(\vec{r}) = \frac{3\pi c^2}{2\omega_0^3}\left(\frac{\Gamma}{\Delta}\right) I(\vec{r}) \tag{2.6}$$

$$\Gamma_{scat}(\vec{r}) = \frac{3\pi c^2}{2\hbar\omega_0^3}\left(\frac{\Gamma}{\Delta}\right)^2 I(\vec{r}) \tag{2.7}$$

Based on these two equations, we can directly infer that a negatively detuned laser beam can produce an optical potential well, capable of trapping the atom in its local intensity maximum. Alternatively, a positive detuning can enable trapping in an intensity minimum. These will be visualised later in this section. Also, the differential AC Stark shift frequency versus scattering rate at any location within the trapping region scales as $\frac{\Gamma_{scat}}{U_{dip}/\hbar}(\vec{r}) = \frac{\Gamma}{\Delta}$, i.e., scales inversely with the detuning. A large detuning enables the trap to be sufficiently deep such that off-resonant scattering events do not lead to atom loss within the back-ground-limited trap lifetimes. Hence, it's common practice to use optical dipole traps which are far-red-detuned from the D Line transition, although at high intensity, to trap $^{87}Rb$ atoms.

The semi-classical picture explains the trapping principle well, but the $^{87}Rb$ atom is in fact a quantum-mechanical multi-level system with the light field acting as a quantum-mechanical perturbation, and a completely quantum-mechanical picture is better suited to frame a theory of trapping, especially if the substructure is resolvable compared to the detuning of the trapping light. The various transitions between the multiple atomic levels are determined by dipole matrix elements

as will be shown now. Consider the ground state $|g\rangle$ of the atom with dipole moment operator $\mu$, and the excited states $|e_j\rangle$s. It is enough to consider the ground state potential for trapping as the atom spends most of its time in that state in the under-saturated condition. The ground state AC Stark shift is then given by the application of non-degenerate second order perturbation theory in the dressed atom picture, as given below:

$$\delta E_i = \sum_{(j\neq i)} \frac{|\langle j|\mathcal{H}_o|i\rangle|^2}{\mathcal{E}_i - \mathcal{E}_j} = \sum_{(j\neq i)} \frac{|\langle e_j|\mu|g_i\rangle|^2}{\hbar\Delta_{ji}}|\vec{E}|^2 = \frac{3\pi c^2\Gamma}{2\omega_0^3} I(\vec{r}) \sum_{(j\neq i)} \left(\frac{c_{ji}^2}{\Delta_{ji}}\right) \tag{2.8}$$

Here, the real transition coefficients $c_{ij}$s are obtained as $\mu_{ij} = c_{ij}\|\mu\|$, satisfying $\sum_{(j,i)} c_{ji}^2 = 1$; $\Gamma = |\langle 5P|\mu|5S\rangle|^2 \frac{\omega_0^3}{3\pi\epsilon_0\hbar c^3}$ is the approximate transition line-width considering only the electronic wave functions, i.e., neglecting the spin-orbit and nuclear spin couplings; and the reduced matrix element $\|\mu\|$ depends only on the decay rate $\Gamma$.

Thus, for purely linearly polarized trap light and fine structure resolvable compared to the trap laser detuning ($\Delta_{g,j} \sim \Delta E_{FS} \gg \Delta E_{HFS} \gg \Delta E_{HFS'}$), we can expand the ground-state energy shift in Eq.(2.8) to obtain the optical potential as:

$$U_{dip}(\vec{r}) = \frac{\pi c^2\Gamma}{2\omega_0^3}\left(\frac{1}{\Delta_{1/2,1/2}} + \frac{2}{\Delta_{1/2,3/2}}\right) I(\vec{r}) \tag{2.9}$$

The $J = \frac{3}{2}$ and $J = \frac{1}{2}$ sub levels have branching ratios (transition co-efficients) $\frac{2}{3}$ and $\frac{1}{3}$ respectively. The quantum mechanical approach takes into account the D line doublet's separate contributions to the AC Stark shift! Similarly, the scattering rate of the trap laser photons is governed by the same dipole matrix elements, and the derivation follows similar perturbative strategy:

$$\Gamma_{scat}(\vec{r}) = \frac{\pi c^2\Gamma^2}{2\hbar\omega_0^3}\left(\frac{1}{\Delta_{1/2,1/2}^2} + \frac{2}{\Delta_{1/2,3/2}^2}\right) I(\vec{r}) \tag{2.10}$$

Of particular importance is that the selection of linearly polarized light for trapping induces equal AC Stark shift in all the Zeeman sub-levels $m_J$ (and consequently $m_F$), as well as equally populates them due to unresolved hyperfine substructure compared to detuning. This leads to uniform trapping potentials and scattering frequency being experienced by all atoms populating any of the magnetic sub-levels in an ensemble.

Now, we can talk about the choice of beam profile suitable for trapping atoms, based on the theory

developed above. We already know that an intensity maximum is a pre-requisite for trapping using red-detuned light. A tightly focussed Gaussian beam far red-detuned to the atomic resonance is the simplest way to confine atoms in 3-D, as will be shown here. Consider a Gaussian beam with power $P$ focused tightly to a spot of $\frac{1}{e^2}$ beam waist $w_0$, at a wavelength $\lambda$. Then the intensity profile is given as:

$$I(\vec{r}) = I(r,z) = \frac{2P}{\pi w^2(z)} e^{\frac{-2r^2}{w^2(z)}} \tag{2.11}$$

where the $\frac{1}{e^2}$ beam radius at longitudinal position $z$ is $w(z) = w_0\sqrt{1+\left(\frac{z}{z_R}\right)^2}$; and Rayleigh range is $z_R = \frac{\pi w_0^2}{\lambda}$. Applying a simple power law scaling and variable separability, substituting Eq.(2.11) into Eq.(2.9) results in an approximate cylindrically symmetric harmonic potential for atoms with temperature $T \ll \frac{U_0}{k_B}$:

$$U_{dip}(r,z) \approx -U_0\left(1 - 2\left(\frac{r}{w_0}\right)^2 - \left(\frac{z}{z_R}\right)^2\right) \tag{2.12}$$

where $U_0 = -U_{dip}(r=0,z=0) = \frac{-Pc^2\Gamma}{\omega_0^3 w_0^2}\left(\frac{1}{\Delta_{1/2,1/2}} + \frac{2}{\Delta_{1/2,3/2}}\right)$ is the trap depth. We can immediately spot that the trap is steeper in the radial direction than the axial, due to azimuthal cylindrical symmetry compounded with the fact that $z_R > w_0$ (even though the beam is focussed to the diffraction limited spot size). This means there is greater confinement available in the radial direction than in the axial direction. More about the trap frequencies in different directions will be discussed in Chapter 4.

The gradient force for small amplitude oscillations about the trap minimum is just the gradient of the harmonic potential given in Eq.(2.12),

$$\vec{F}_{dip}(\vec{r}) = -\vec{\nabla}U_{dip}(\vec{r}) = -\frac{4U_0}{w_0^2} r\,\hat{r} - \frac{2U_0}{z_R^2} z\,\hat{z} \tag{2.13}$$

The scattering force is the product of the scattering rate given in Eq.(2.10) and the momentum $\hbar\vec{k}$ imparted during each scattering event,

$$\vec{F}_{scat}(\vec{r}) = \hbar\vec{k}\left(\frac{\Gamma_{scat}(\vec{r})}{2\pi}\right) = \frac{\hbar}{\lambda}\Gamma_0\, e^{\frac{-2r^2}{w^2(z)}}\,\hat{z} \tag{2.14}$$

Ratios of the amplitude of the restoring force to the frictional force $\frac{F_{dip}}{F_{scat}}$, and to the gravitational force experienced by the atom $\frac{F_{dip}}{mg}$, are both of the order $\sim 10^4$. Hence, a vertical or horizontal tweezer doesn't significantly change the location of the atoms in the tweezer, and this allows considerable leniency in the tweezer optics geometry. In conclusion, the intensity maximum occurs precisely at the focus $()r = 0, z = 0)$. The off-resonant trap light scattering rates are negligible for large detunings comparable to the fine-structure energy spacings, so the axial confinement is almost centered at the focus itself despite the momentum imparted in the beam propagation direction. If the trap is loaded from a Magneto-Optical Trap (MOT) where the atoms are pre-cooled to about few tens of micro-Kelvin, a trap depth of 1 mK along with cooling light is sufficient to hold the atoms for a sufficient amount of time (few seconds) to carry out quantum protocols.

To summarise, we require a far-red detuned, tightly focussed, and linearly polarized Gaussian beam to constitute a successful optical tweezer for neutral $^{87}Rb$ atoms. This situation is visualised in Fig.2.1(a), while Fig.2.1(b) demonstrates a possibility of trapping using far blue-detuned bottle laser beam in the first Laguerre-Gaussian mode. This is achieved by trapping in the intensity minima of the doughnut shaped potential.

The ability to generate multiple re-configurable optical dipole traps/tweezers is granted by the use of diffractive optical elements, as discussed previously in Section 2.1. For a 1-D array with trivial rearrangement, Acousto-Optic Deflectors (AOD) are sufficient, whereas large scale static 2-D arrays with pick-and-drop-type rearrangement facility can be generated via a hybrid architecture consisting of Spatial Light Modulators (SLM) and AODs. In the next couple of sub-sections, the working principle of these devices will be explained.

### 2.2.2 Array Generation Techniques – Acousto-Optic Deflector

The 'Acousto-Optic effect' is the periodic spatial alteration of the refractive index of a material subjected to mechanical strain introduced by acoustic waves propagating through it. Incident light is therefore Bragg diffracted by an effective grating generated by the sound column in the material. An AOD is a high-speed beam steering device assembled using a crystal with favourable properties such as high Acousto-Optic figure-of-merit $(M_2)$, high birefringence, low acoustic attenuation, high transparency, etc., which is attached on one end to an RF-driven piezo-electric transducer. For visible light and NIR, the widely accepted choice of crystal is Tellurium Dioxide $(TeO_2)$ due to its exceptionally high $M_2$ in this spectral range, and excellent birefringence along with a very low acoustic wave velocity (616 $\text{ms}^{-1}$) in the slow shear wave direction [110].

Now, consider a light beam of width $w$ and wavelength $\lambda$ incident at an angle $\theta_i$ to the AO crystal's optic axis $\hat{z}$ (this axis is defined perpendicular to [110]). The piezo is driven by an RF with fixed

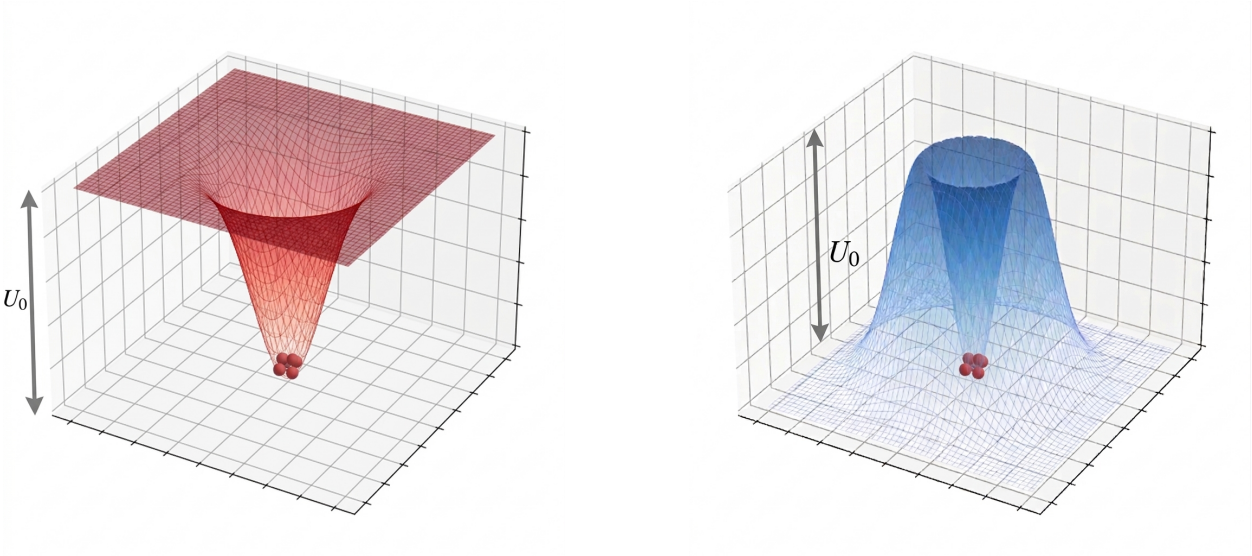


(a) (b)

Figure 2.1: (a) Red-detuned trap implemented using a Gaussian beam profile; (b) Blue-detuned trap implemented using a $LG_{01}$/ doughnut beam profile.

frequency $F$, and the acoustic waves are propagating at a small angle $\alpha$ to [110], with a wave velocity $V = V(\alpha)$. Since the crystal is optically active and birefringent, there is a separation of refractive indices for the two polarizations (slow and fast) of light, $n_1(\theta)$ and $n_2(\theta)$ (anisotropic regime). Operation in the shear mode renders the polarization of the diffracted beam rotated by 90° (i.e., the diffracted beam is in the slow mode if the incident beam is in the fast mode). In view of this phenomena, the diffracted beam exits at an angle $\theta_d$ such that it satisfies the Anisotropic Bragg diffraction conditions imposed by pseudo-momentum conservation: $\vec{k}_i + \vec{K} = \vec{k}_d$ and $\nu_i \pm F = \nu_d$, where $|\vec{k}| = \frac{2\pi n_\theta}{\lambda}$ is the wave vector of the incident and diffracted beams with their corresponding refractive indices, and $|\vec{K}| = \frac{2\pi F}{V}$ is the wave vector of the acoustic wave. For a given center driving frequency $F_c$, the diffracted beam is perpendicular to [110] for some particular $\theta_i = \theta_{Bragg} = \frac{\lambda F}{2V}$, and displays Bragg degeneracy due to tangential phase matching. Thus, it undergoes another diffraction and exits with $\theta_d = -\theta_{Bragg}$. For a small bandwidth $\Delta F$ about this center driving frequency $F_c$, the optical response remains relatively flat as $\frac{\partial \theta}{\partial F}\Big|_{\theta_i = \theta_{Bragg}} = 0$.

For an AOD, the AO crystal is cut such that the resultant optic axis $\hat{z}$ corresponds to a wide optical flatness ($\Delta F$) about the chosen $F_c$, whilst still maintaining a high diffraction efficiency $\eta(F)$. For a multi-tone RF drive supplied within the bandwidth, the AOD diffracts the incident beam into multiple first-order diffraction spots, by virtue of the superposition principle. The number of such resolvable spots is given as $N = \frac{w\Delta F}{V} = \tau \Delta F$, also known as the time-bandwidth product, where $\tau$ is the transit time of the acoustic wave across the beam width. The construction and working of the

AOD is displayed in Fig. 2.2.

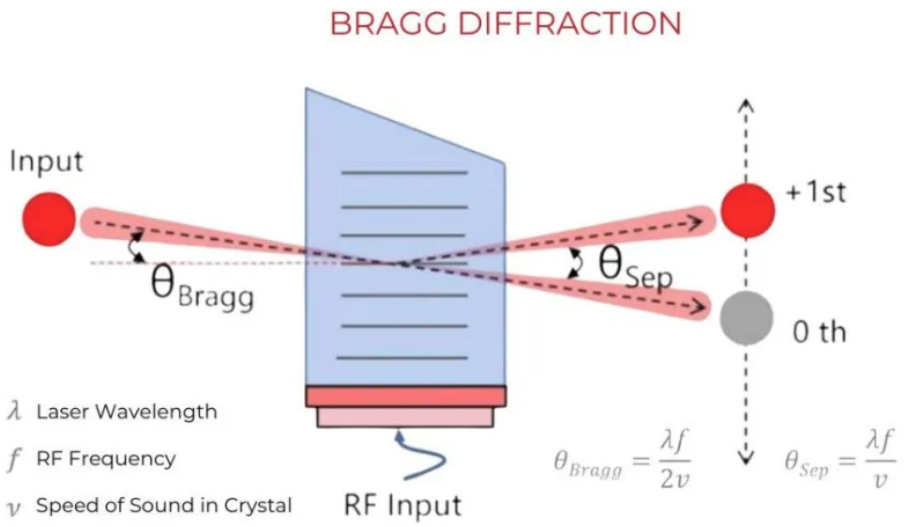


Figure 2.2: Acousto-Optic Deflector Working Principle.

Hence, the use of a 2-axis AOD (2 separate AO crystals aligned orthogonal to each other) allows generation of multiple diffraction spots in 2-D ($\sim 10 \times 10$) from a single high powered Gaussian beam, and these spots are simultaneously reconfigurable in space due to the ability to stream RF frequency sweeps in time domain via the use of Arbitrary Wave-form Generators (AWG). Optimisation of the trade-off between transit time ($\tau = \frac{w}{V}$) and maximum deflection aperture ($\Delta\theta = \frac{\lambda\Delta F}{V}$) allows high-speed rearrangement protocols of optical tweezers to be carried out while maintaining considerable clearance between neighbouring tweezers.

An Acousto-Optic Modulator (AOM) operates according to the same principle stated here but offers faster switching times, making it suitable for amplitude modulation, frequency shifting, or rapid switching of the diffracted order. It trades off very low transit times for a reduced deflection aperture, rendering it unusable for large-array generation. However, small-scale timeshared arrays in 1-D and 2-D can be realised. More about this will be shared in Chapter 4.

### 2.2.3 Array Generation Techniques – Spatial Light Modulator

Given a target intensity profile (target amplitude) and an incident beam initial amplitude and phase profile, a phase hologram can be arrived at iteratively (Weighted Gerchberg Saxton Algorithm), which when superposed onto the incident wavefront before a subsequent Fourier transform, yields the desired target intensity pattern. A Phase-Only-SLM works on the principle of modifying the phase profile of an incident wavefront. The SLM is constructed by sandwiching nematic Liquid

Crystals (LC) molecules between a transparent, electrode-coated cover glass and a pixelated, reflective, and CMOS-addressed electrode backplane. The LC molecules are birefringent and their voltage-controlled orientation non-linearly but monotonically corresponds to a certain value of extra-ordinary refractive index ($n_e(V_B)$). Thus, an in-phase light wavefront which is linearly polarized parallel to the extraordinary axis of the LC material and incident onto the SLM screen, reflects off it with a modified phase profile, due to variable optical path delay offered by each pixel based on the voltage bias ($V_B$) applied to it. This generates a relative phase difference between adjacent pixels, that is electronically tuneable up to one full wave, enabling precise phase modulation. This situation is visualised in Fig.2.3.

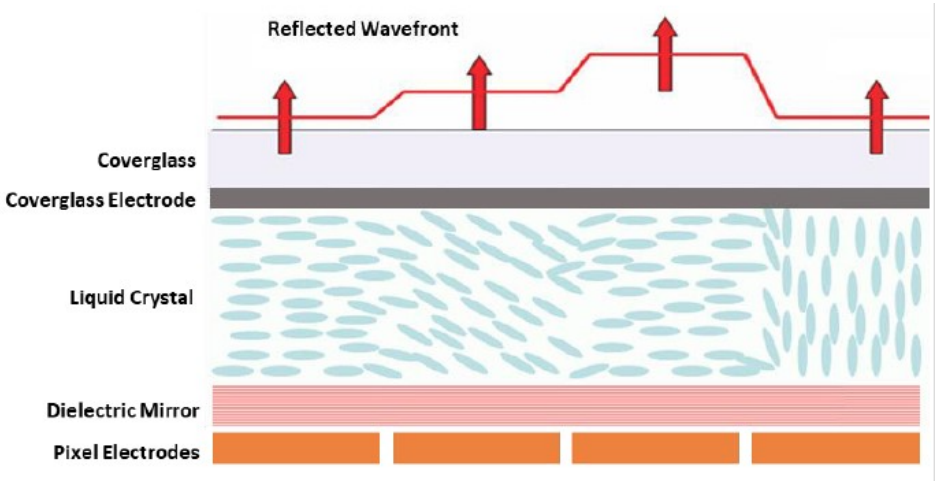


Figure 2.3: Spatial Light Modulator Working Principle.

An $N \times N$ array of optical tweezers in the focal plane of a high-NA lens sets the target diffraction pattern amplitude, i.e., an array of equally-spaced spots with Gaussian intensity profiles. Knowing this, a feedback-enabled application of the WGS algorithm can modify the phase profile of a linearly polarized, in-phase, Gaussian beam incident on the SLM display to obtain the desired target pattern. The ability to precisely control the phase with excellent resolution provided by the SLM ($1024 \times 1024$ pixels) allows us to possibly generate up to a million traps ($N = 1000$). A drawback, however, is the static nature of the trap, as SLMs cannot dynamically move the traps sufficiently fast, due to the innate feedback loop-based nature of the algorithm used to generate the traps. Hence, a moving trap whose trap depth can be increased or decreased to pick or drop a single atom respectively needs to be superposed onto the existing static array. Such a trap is easily generated and manipulated using an AOD. This hybrid architecture allows rearrangement in 2-D arrays.

### 2.2.4 Collisional Blockade

There exist multiple strategies in the literature to realize single atoms within an optical dipole trap. A few loading strategies are – Superfluid-to-Mott insulator transition, Rydberg blockade-assisted blow away, Penning ionization, and Light-Assisted Collision-based blockade (LAC). Of these, the most preferred is a loading from a pre-cooled cloud of atoms, such as a Magneto-Optical Trap (MOT), into the tweezer using LAC in the collision blockade regime. The collisional blockade regime for $^{87}Rb$ atoms is characterised by two pre-requisites: a fairly deep trap with sub-/near micron-beam waist, and light field resonant with the $D_1/D_2$ transition. The theory behind LAC based single-atom loading will be detailed below. [20, 21].

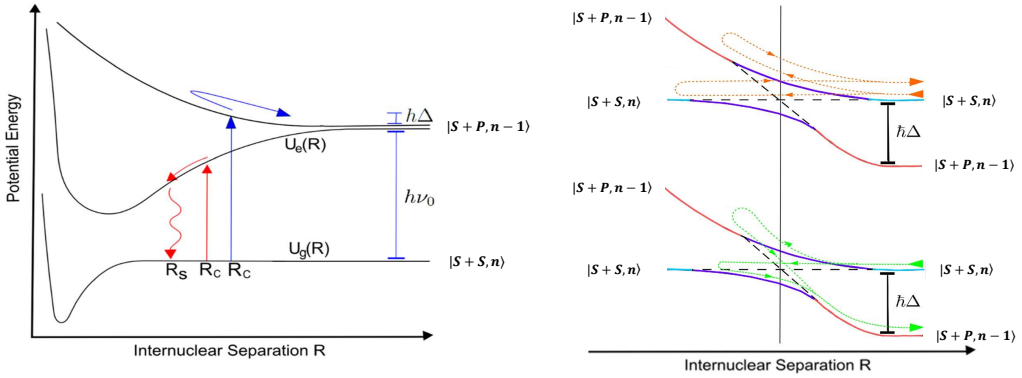


(a) (b)

Figure 2.4: (a) Condon radius for excitation to the molecular potential and subsequent inelastic collisions; (b) Dressed state picture in LZ Formalism for LAC. Adapted from [19]

Consider two ground state atoms in close proximity, whose collective wave function is given as $|S + S\rangle$. The long-range asymptote of their potential scales as $V_g = \frac{-C_6}{R^6}$ due to the attractive London dispersion interaction. A centrifugal barrier $V_c = \frac{l(l+1)\hbar^2}{2\mu R^2}$ arising as a consequence of relative rotational motion between two the atoms can be ignored as the barrier occurs at much larger distances than the tight trap's beam waist. The long-range asymptote of the first molecular excited state $|S + P_{3/2}\rangle$ scales as $V_e = \hbar\omega_0 \mp \frac{C_3}{R^3}$ due to the stronger dipole-dipole interactions ($\omega_0$ is the $5S_{1/2} - 5P_{3/2}$ transition frequency). These potentials are either attractive or repulsive based on the relative phase of the approaching dipoles. When a collision beam of frequency $\omega_L$ detuned by an amount $\Delta_L$ with respect to the light-shifted resonance is shone on the trap, the two atoms confined within the trap volume is excited to either the attractive or the repulsive molecular potentials based on the sign of the detuning (red-detuned and blue-detuned collision beam respectively). The excitation occurs precisely at the Condon radius $R_C$ which corresponds to a potential energy difference equaling the energy $\hbar\omega_L$ supplied by the resonant photons, as shown

in Fig.2.4(a). The probability of the atoms exploring the Condon separation is enhanced due to the tight trap constraint. Of interest to note is that for typical excitations, the Condon radius is sufficiently far removed from the repulsive Coulomb regime that the ground state potential can be treated to be a constant.

As the atoms roll down the potential hill (collision in case of attractive potential and deflection in case of repulsive potential), the kinetic energy $\Delta E_K$ gained is distributed amongst themselves before a spontaneous emission of a photon takes place at a lower frequency than the absorbed photon. The energetics of this inelastic collision is as follows:

**Red-detuned collision beam:** The maximum kinetic energy $\Delta E_K$ obtainable rolling down the attractive potential has an upper bound set by the depth of the potential. In the dressed state picture of Landau-Zener formalism , an inelastic collision results in the asymptotic initial state $|S + S, n\rangle$ transitioning over to the final state $|S + P, n - 1\rangle$ as shown in Fig.2.4(b). For cold atoms in the temperature range of a few tens of micro-Kelvins, the velocity of approach is so slow that multiple absorption-emission cycles can be completed by the time the two atoms come sufficiently close together to reach the minima of the attractive potential. Thus, the inter-atomic distance $R_S \leq R_C$ at which the spontaneous emission occurs sets the total energy gained during the inelastic collision at $\Delta E_K = V(R_C) - V(R_S)$.

**Blue-detuned collision beam:** The maximum kinetic energy $\Delta E_K$ obtainable rolling down the repulsive potential has an upper bound set by the detuning of the collision light, $\Delta E_K \leq \hbar\Delta_L$. As before, the inelastic collision results in the asymptotic initial state $|S + S, n\rangle$ transitioning into the asymptotic final state $|S + P, n - 1\rangle$, as shown in Fig.2.4(b).

Based on these energetics, there exist the following outcomes for the trapped atoms:

1. Both atoms are ejected from the trap post collision due to $\Delta E_K > 2U_0$, rendering the trap empty. This is termed the $2 - 0$ loss channel.

2. Only one atom is lost from the trap due to unequal sharing of the gained kinetic energy ($U_0 < \Delta E_K < 2U_0$). The remaining atom is cooled back down by the probe cooling light. This is the $2 - 1$ loss channel.

3. No atom is lost from the trap either due to equal sharing of the gained kinetic energy ($U_0 < \Delta E_K < 2U_0$) or because it is insufficient to eject either of the atoms ($\Delta E_K < U_0$). Both the atoms cool back down due to the probe cooling light.

The occupation number of the trap can be thus modelled mathematically as:

$$\frac{dN}{dt} = R - \alpha N - \beta N(N-1) - O(N^3) \tag{2.15}$$

where $R$ is the loading rate of atoms into the tweezer, $\alpha$ is the one-body loss coefficient due to collisions with background vapour atoms around the tweezer, $\beta$ is the two-body collision coefficient and other higher order loss channels are tremendously suppressed due to the typically weak operational loading rate into the trap as well as the tightness of the trap.

Looking at Eq.(2.15), we can see that provided optimised loading from a MOT cloud along with sufficient background cooling light from the 3 pairs of counter-propagating MOT beams, we can carefully operate within a parameter space for which the $2-0$ or $2-1$ loss channels largely dominate during the repeated cycles of inelastic collisions induced by the background collision light (LAC). This parameter range, typically described by a weak/sub-critical loading rate into a very tight trap, along with highly red-/blue-detuned collision beams and ultra-high vacuum conditions (i.e., $\alpha \ll R \ll \beta$), is termed as the 'collisional blockade regime' in literature. One immediately notices that it renders the occupation probability of a tight trap within the sub-Poissonian regime, where $\langle N_{occ} \rangle \leq 1$ and $0 < P(N = 1) \leq 1$. Moreover, no more than one atom can simultaneously exist in a tight trap given the above conditions, due to the rapid trap loss probability. Hence, we have in our hands a mechanism to load and trap, although probabilistically, single neutral $^{87}Rb$ atoms in an optical tweezer array.

## 2.3 Rubidium-87

Since the whole thesis revolves around $^{87}Rb$, and its energy profile to address laser frequencies and experimental methods will be frequently used, now is a good time to shed some light on this neutral atom, specifically its $D_2$ transition hyperfine structure.

Rubidium is an alkali metal with an atomic number of 37, and exists as a soft solid with a density of $1.53 \times 10^3$ kgm$^{-3}$ and a vapour pressure of $3.92 \times 10^{-7}$ Torr at 25 °C. Rubidium oxidizes violently in air and water; hence care must be taken while handling Rb ingots or pills as a source for atomic physics experiments. The stable isotopes of rubidium are $^{85}Rb$ and $^{87}Rb$, which have natural abundances of 72.17 % and 27.83 % respectively.

$^{87}Rb$ has an atomic mass of 86.909 amu. It has a half-integer nuclear spin of $\frac{3}{2}$. Thus, the interaction of the nuclear magnetic dipole moment with the magnetic field due to total electronic angular momentum leads to hyperfine splitting in its energy profile. The ground-state $5^2S_{1/2}$ has two hyperfine levels $F = 1$ & $2$ separated by a hyperfine splitting $\Delta E_{HFS} = 6.834$ MHz.

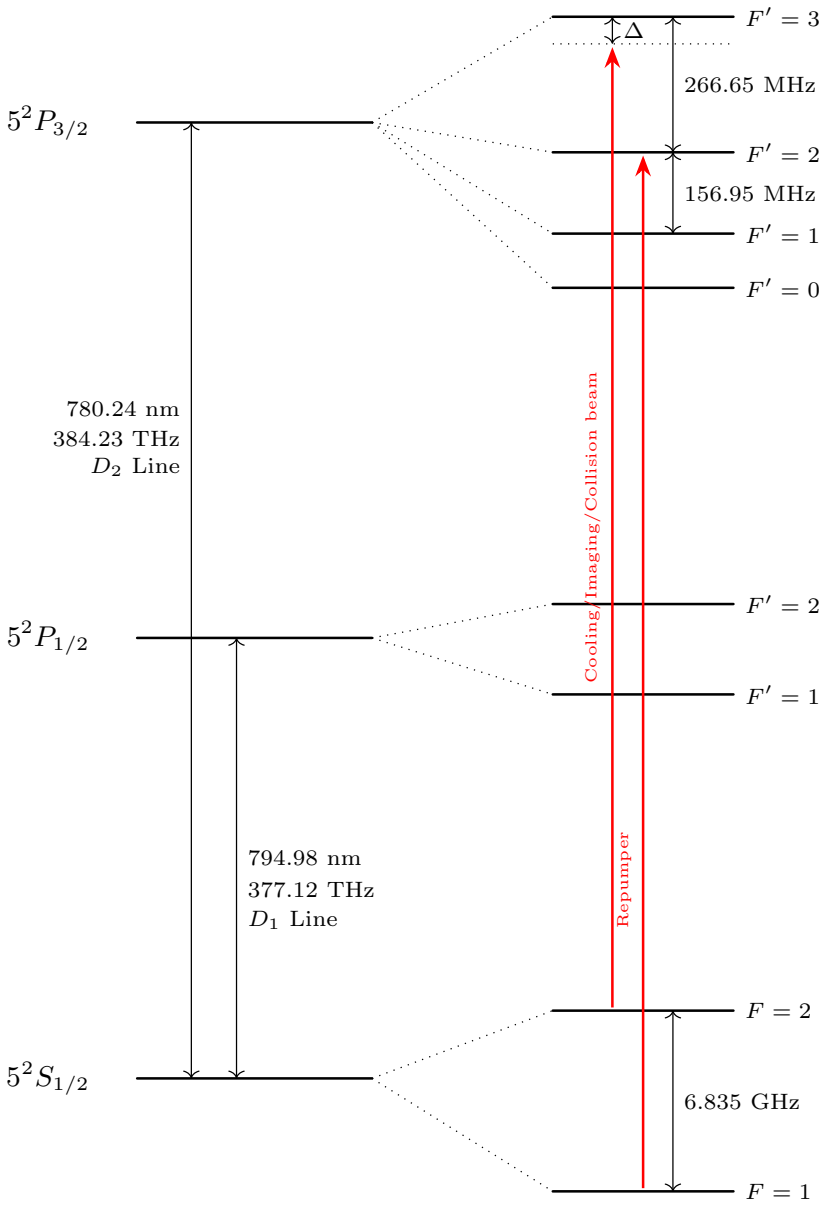


Figure 2.5: $^{87}Rb$ Energy Levels and Laser Frequencies

The strong electric dipole-allowed cycling $D_2$ transition $5^2S_{1/2} \longrightarrow 5^2P_{3/2}$ at 780 nm facilitates laser cooling and trapping of $^{87}Rb$. In literature as well as in this thesis, the closed and strongest $D_2$ transition $F = 2 \longrightarrow F' = 3$ is used in the Zeeman slower and MOT cooling stages, as well as for the light assisted collisions in the tweezer and fluorescence imaging of the atoms. The lasers are typically slightly red-detuned to this transition ($\sim 2\Gamma - 5\Gamma, \Gamma = 6.07$ MHz) for Doppler cooling, polarization gradient cooling and fluorescence imaging; however there also exist blue-detuned LAC as was described earlier in Section 2.2.4. However, this transition is still leaky, as some atoms de-pump into the dark ground-state hyperfine level $F = 1$ through off-resonant coupling to the $F' = 2$ hyperfine state. To pump atoms back into the $F = 2$ level, the re-pump lasers slightly red-detuned to the $D_2$ transition $F = 1 \longrightarrow F' = 2$ are used. The energy level diagram along with the hyperfine structure and typical laser frequencies is presented in Fig.2.5.

# Chapter 3

# Experimental Setup

In this Chapter, the experimental setup of the optical tweezers and integration with the BEC system, along with the miniature assembly will be demonstrated. Additionally, an attempt at constructing a miniaturized portable assembly for single neutral atoms traps will also be shared.

## 3.1 Experimental Setup – Optical Tweezer 1-D Array

The current Rubidium BEC readily allows the direct integration of tweezer optics to enable single-atom trapping, with a few minor adjustments to the probe beam path and camera imaging path. For more information on the laser cooling of $^{87}Rb$ atoms and the formation of the optical molasses and the MOT, refer to the Ph.D. theses of previous lab members (Sumit Sarkar [22], Sunil Kumar [23]).

The following describes the laser delivery systems apart from those required for the MOT (Zeeman slower, cooling and repumper light). A Toptica TA pro laser system at 813 nm coupled to a single-mode fiber delivers the trapping laser. Inside the Rb optical bench, a Toptica TA pro laser system SAS-locked to the $F = 2 \longrightarrow F' = 2$ $D_2$ transition and a DL 100 laser system SAS-locked to the $F = 1 \longrightarrow F' = 1$ $D_2$ transition is coupled to the same single-mode fiber post double-pass AOMs operating at 127 MHz and 80 MHz respectively. These deliver about 6 mW of probe imaging light and 12 mW of probe repumper light respectively. All the fibers output the light through an $f = 10$ mm Schäfter-Kirchhoff fiber collimator, collimated at 0.75 mm in the $TEM_{00}$ mode.

I will now describe the tweezer optics. A wavelength filter cleans the trapping laser spectrum and the beam is passed through an AOD configured to output the -1 diffraction order for maximum efficiency centered around 25 MHz. An RF multi-tone generated by a Spectrum Arbitrary Waveform

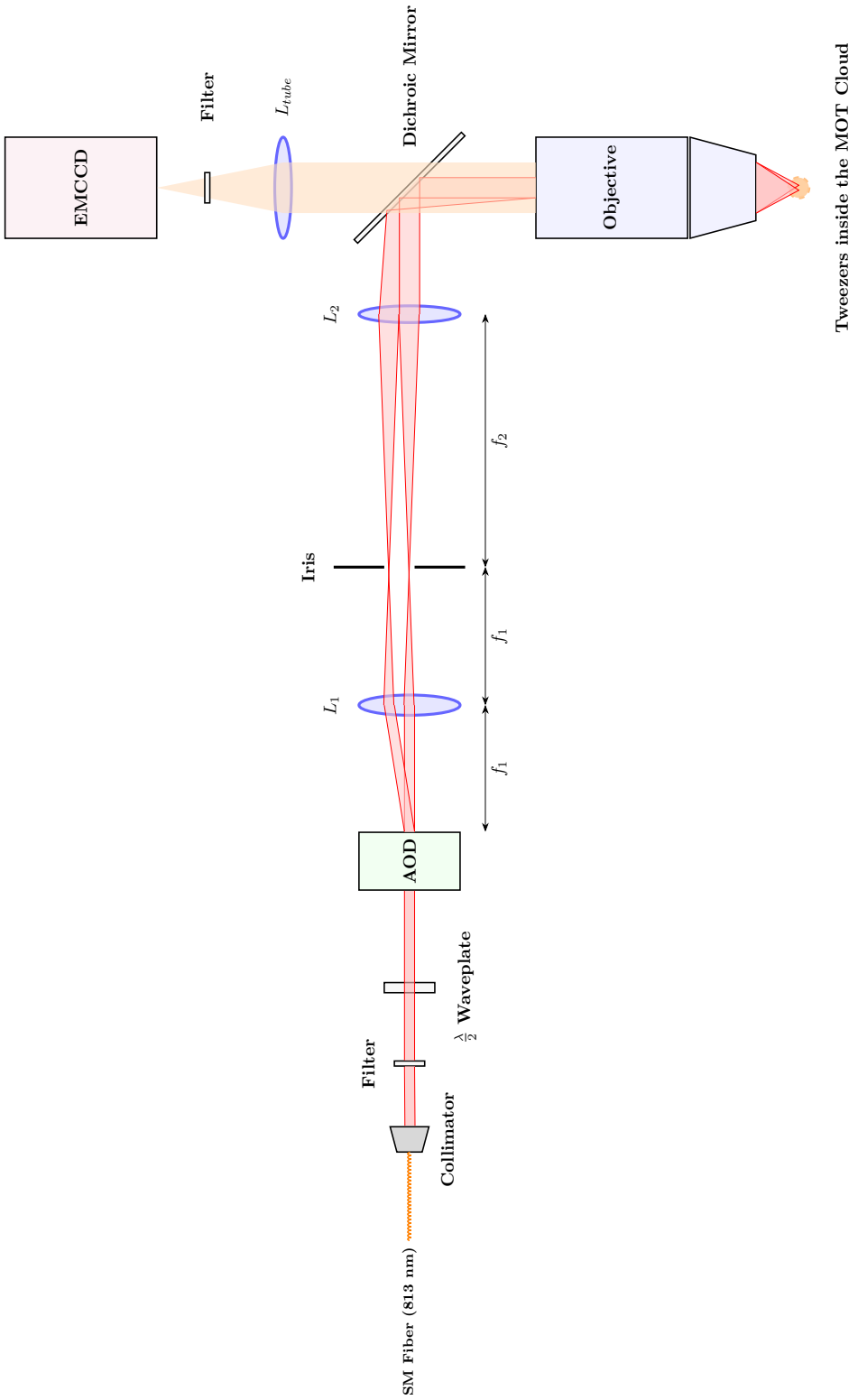


Figure 3.1: Tweezer delivery ($0^{th}$ & $1^{st}$ orders) and imaging schematic

Generator (AWG) and amplified by a 2 W Amplifier drives the AOD to produce multiple diffracted beams. These diffracted beams are expanded by a $\sim 6:1$ expander and reflected via a dichroic mirror to fill the back aperture of a Mitutoyo M Plan Apo 10X $\infty$-corrected microscope objective. Telecentricity of the expander is executed by conjugating the back-aperture of the objective with the interaction zone of the AOD, i.e., the AOD is at distance $f_1$ away from the first lens and the back aperture is at distance $f_2$ from the second lens, while an iris blocks the undiffracted zeroth order at their common focus. Thus, the objective focuses each beam to the diffraction limited spot-size at its working distance, essentially forming an array of optical tweezers centered inside the MOT. The conjugation ensures that an angular separation of different diffracted beams at the AOD corresponds to a spatial separation in the focal plane of the objective. Thus a $1 \times N$ array is easily generated by driving one of the axes of the AOD with an equi-spaced N-tone RF centered about the operational center frequency. Despite the various optical losses, the tweezer optics can deliver upto 50 mW of cw trapping light into each trap inside the vacuum chamber, depending on the number of traps generated.

The probe cooling and repumper lasers serve as the imaging-cum-cooling beams and also as the collision/LAC beam during loading of the traps. They are expanded by a factor of two and sent into the vacuum chamber and retro-reflected along the vertical Z axis by co-propagating them with the vertical MOT beam pair, while the objective forms the tweezers in the horizontal X-Y plane. This is done to significantly reduce the scatter from probe light along the horizontal plane and improve the SNR of the imaging. These beams are made to pass through the MOT first by observing the point of destruction of the cloud, and then adjusted to pass through the location of the tweezers by observing the atom fluorescence induced by the probe light.

The imaging is carried out by collecting the fluorescence of the atom array through the large numerical aperture of the same objective used to generate the traps. The collimated atom fluorescence light is passed undeflected through the dichroic mirror and is focussed onto an Andor iXon Ultra EMCCD camera post multiple wavelength filters. For ease of initial optical alignment and imaging, a polarising beam splitter (PBS) diverts the initial trap beam power into an un-expanded path termed the 'tracer'. This path merges again with the expanded tweezer beams and underfills the back aperture of the objective, thus forming an optical dipole trap with a relaxed beam-waist that is able to load a large number of atoms and thus produce very high and easily detectable fluorescence. The schematic diagram for the tweezers is shown in Fig.3.1. The entire integrated setup and the optical bench is displayed in Fig.3.2(a) and 3.2(b) respectively.

The monitoring station is composed of two PCs – one to serve as the digital and analogue master control over the laser AOM's, frequency lock-ins, high-speed shutters, atomic beam valve,

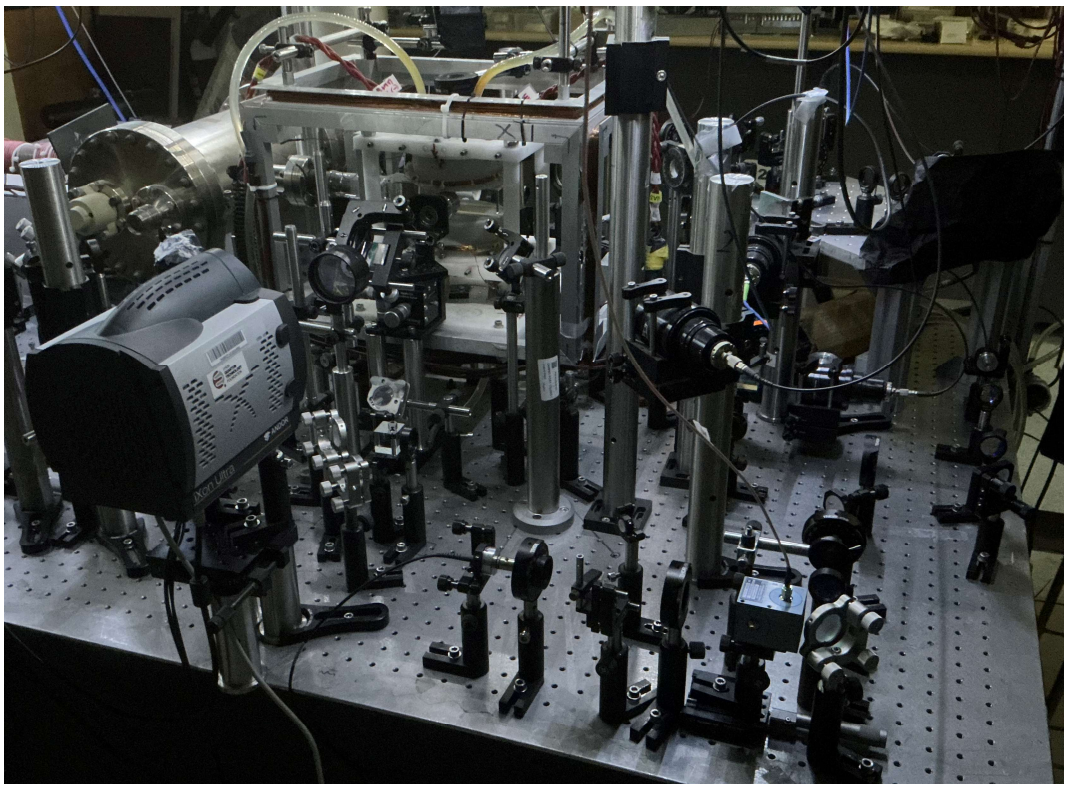

(a)

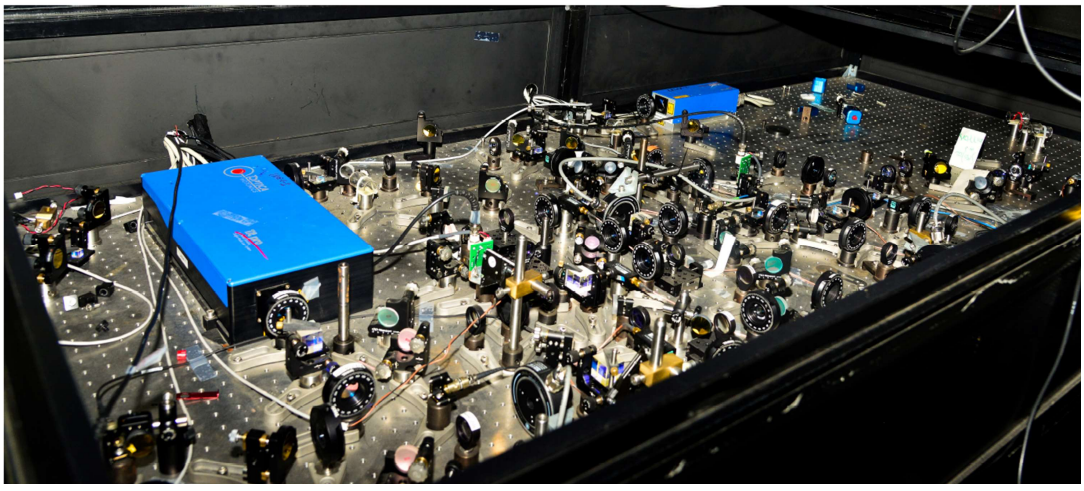

(b)

Figure 3.2: (a) Optical tweezers setup; (b) Optical bench for laser delivery (adapted from [22])

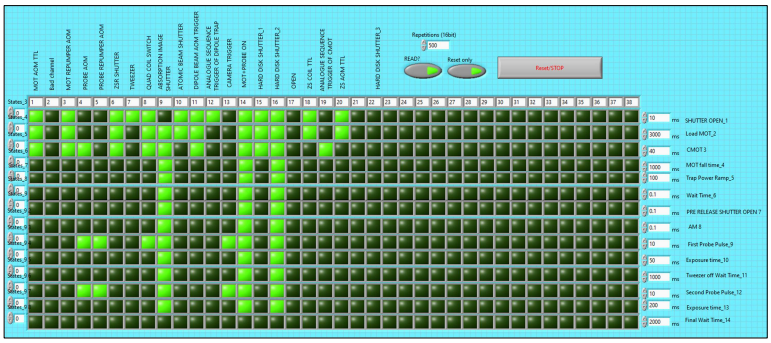

(a)

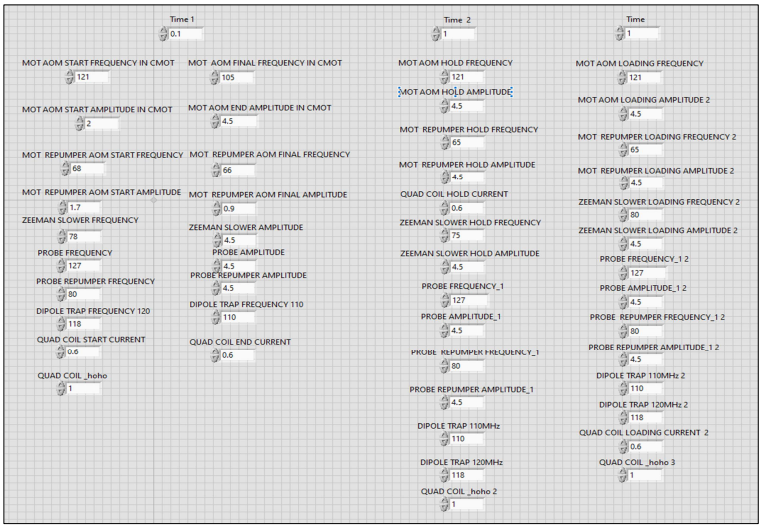


(b)

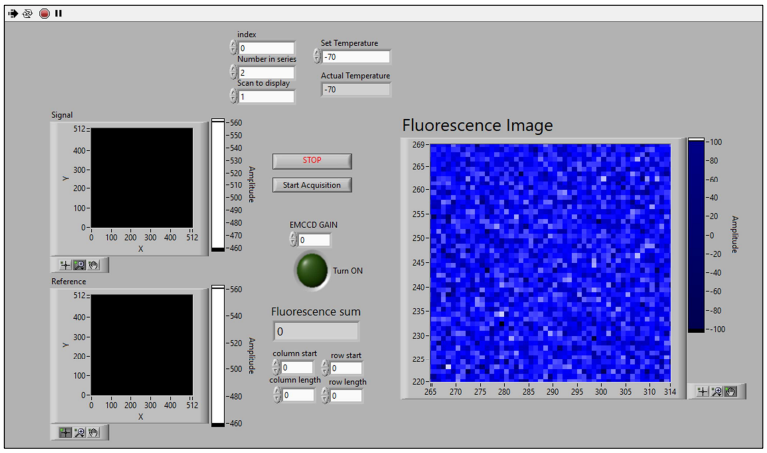


(c)

Figure 3.3: (a) Digital Output Programme for controlling sequence and timings; (b) Analogue Output Programme for master control over detunings and amplitudes; (c) Atom Array Grabber for data acquisition.

quadrupole field coil currents and the timings involved therein; another to acquire the fluorescence data from the EMCCD through its dedicated driver card and process it in a LabView environment for measurements, and also control the AWG via a simple Python script. The display screens are shown in Fig.3.3(a), 3.3(b), and 3.3(c).

## 3.2 Miniature Platform

Here, I will describe a prototyping attempt at a miniaturized and portable assembly for the neutral atom platform. The necessary hardware to create a minimalist but functional science chamber for the trapping of single atoms include a small vacuum cell, an intermediate capacity ion pump capable of reaching UHV, a getter material as the $^{87}Rb$ source, the laser systems for the trap, MOT and imaging as described in Section 3.1, and finally the MOT + Tweezer optics. Other accessories include a Turbo-Molecular Pump (TMP) for the initial pump-down and bake-out, an optional ion gauge for monitoring the internal vacuum level, a power supply for heating the getter, and a PC for master control and data acquisition. With this pruned list, the science chamber is assembled as follows –

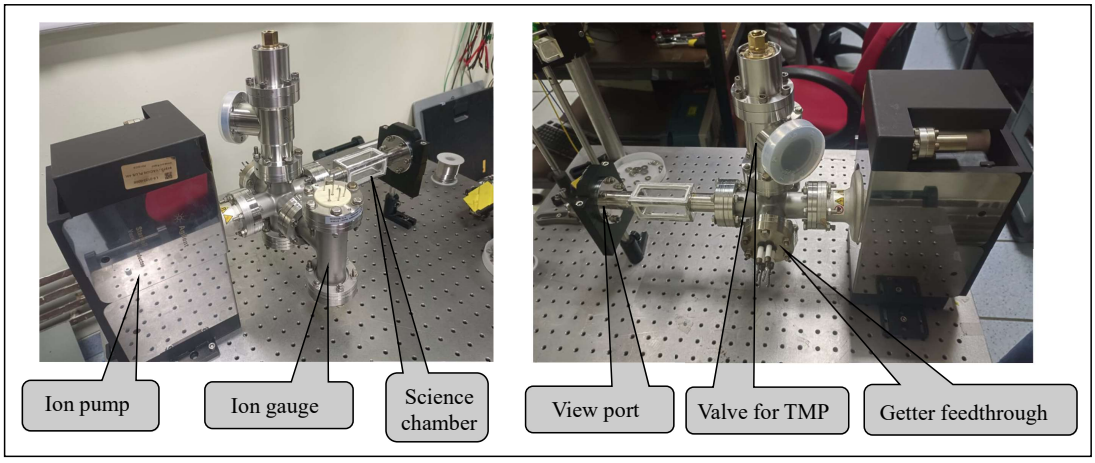


Figure 3.4: Miniature assembly and its components

A home-made vacuum cell is built by gluing four UHV tolerant glass slides (25 mm×75 mm×1 mm) to an SS-316 metallic frame (40 mm × 40 mm × 85 mm) using a UHV-grade epoxy like Torr Seal. An Agilent VacIon Plus 40 pump with a 34 $Ls^{-1}$ capacity and ability to pump down to below $10^{-11}$ mbar is the choice of ion pump used in this design. A wire-shaped AMD *Rb* getter from SAES is soldered onto a vacuum electrical feed-through flange, which can readily dispense Rb vapour upon

pulsing a few amperes of current from a constant current source. An Agilent UHV-24 Bayard-Alpert ion gauge tube is used to monitor the UHV. Finally, these components are all connected to a central ConFlat 6-way cross using copper gaskets, as shown in Fig.3.4. An additional T-valve for the TMP, a viewport for the science chamber and blank flanges are also used to seal the unused ends. The use of flipper mirrors inside the optical desk enables the toggling of the same lasers between the main *Rb* BEC setup and the mini setup. However, the tweezer and MOT optics were not laid out initially to allow the long bake-out process. The outcome and shortcomings of this setup will be discussed in Chapter 4 and 5.

# Chapter 4

# Methods and Results

This chapter will focus on the methods used to characterise the traps and capture the atom loading statistics and provide the results obtained. Later, an attempt to generate a one-dimensional array of tweezers using AOD is also described.

## 4.1 Trap and Device Characterisations

### 4.1.1 Preliminary Beam-Waist Characterisation

A rough preliminary estimate of the tweezer beam-waist needs to be obtained before-hand to get a better idea of whether we operate within the collisional blockade regime or not. To do this, a replica of the tweezer optics on a test optical bench is set up. Here, a reference silicon chip with pre-measured microscopic architecture is imaged by the objective and a tube lens onto a Basler CCD camera. A PBS in combination with a quarter wave-plate allows the imaging of the focussed Gaussian beam reflected from the surface of the same chip. This toy setup is displayed in Fig.4.1(a).

Thus, a calibration of the camera pixel size against the microscopic reference chip architecture is performed, for the specific magnification provided by the imaging tube lens ($f = 200$ mm). It is determined to be around 0.22 $\mu$m/px. A Gaussian fit to the measured line profile of the tweezer at focus gives a beam waist of 8.04 px. Thus, with the over-filled $\infty$-corrected microscope objective with $NA = 0.28$, working distance $WD = 34$ mm and at $\lambda = 813$ nm, the tweezer beam waist is measured to be about 1.77 $\mu$m.

This result agrees very well with the theoretical diffraction-limited resolution of $w = \frac{0.61\lambda}{NA} = 1.77\ \mu$m. With the glass chamber wall of the vacuum cell in between, the tweezer focus is shifted

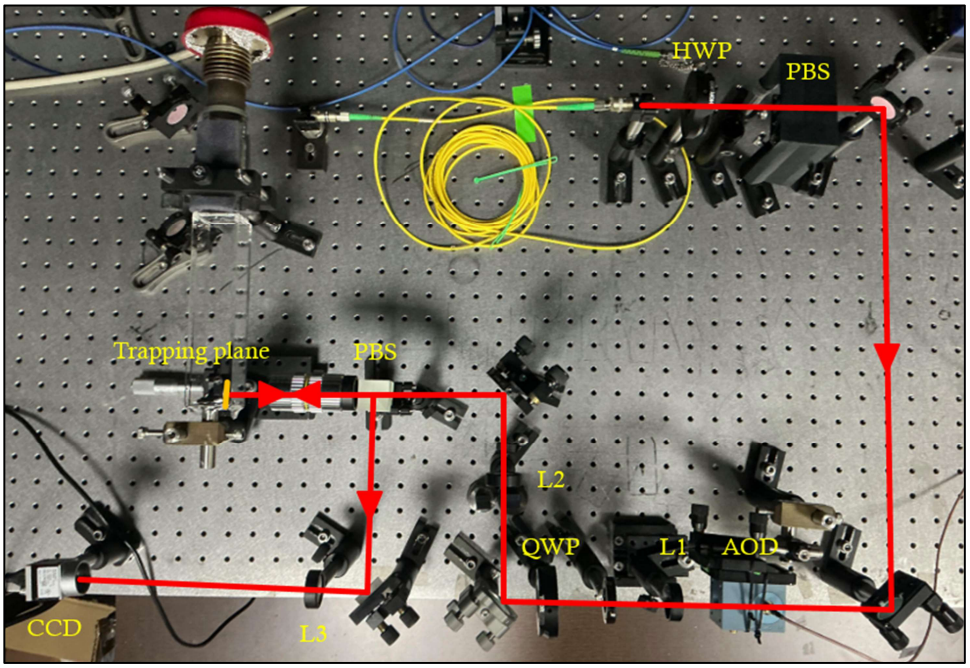


(a)

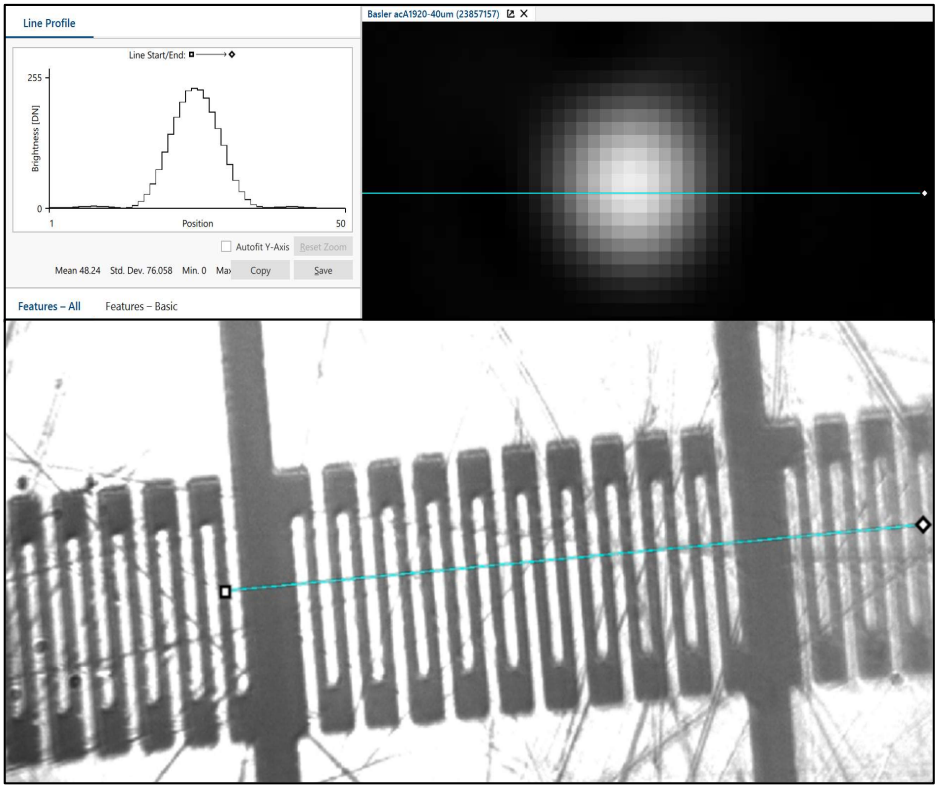


(b)

Figure 4.1: (a) Toy Setup of Optical Tweezers; (b) Calibration using Si chip and beam waist measurement.

away by about 1.2 mm and the beam waist relaxes a bit to 1.80 $\mu$m. This data needs to be taken into consideration while positioning the objective with respect to the MOT cloud.

### 4.1.2 AOD Output

The output of the AOD needs to be reasonably Gaussian to conform to the trapping theory put forth in Chapter 2 previously. Due to the uneven diffraction efficiency of the AOD, the power in the various tones as well as the beam profiles are expected to have variation.

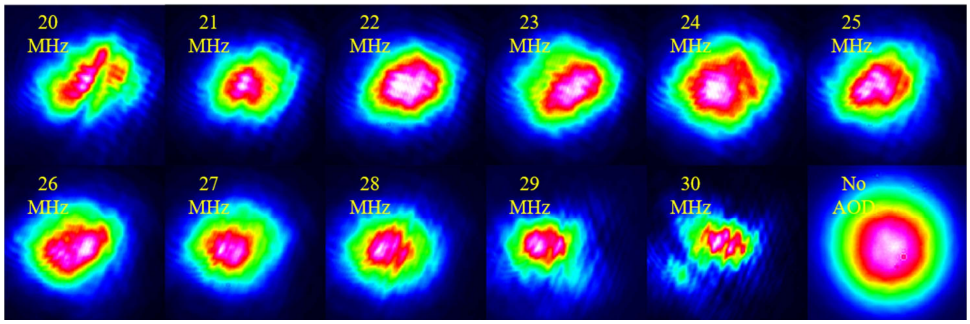


(a)

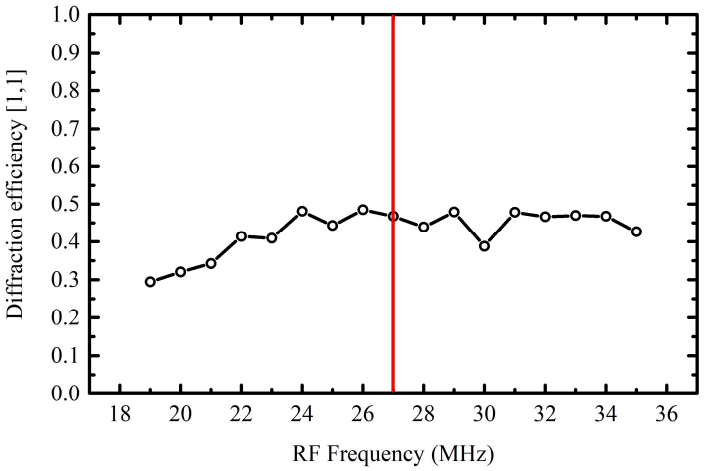


(b)

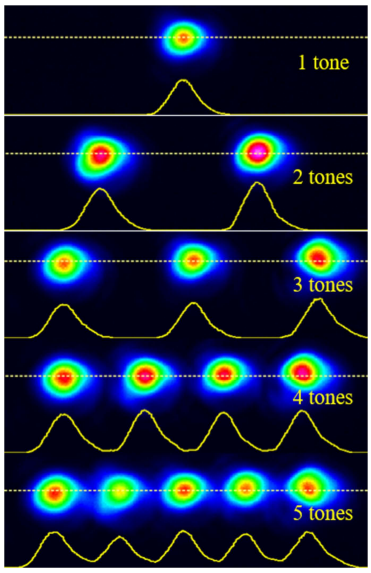


(c)

Figure 4.2: (a) Beam profiles from 20-30 MHz; (b) AOD Diffraction Efficiency in first order; (c) Amplitude compensated multi-tone profile.

The beam profiles of the array with a multi-tone drive are obtained using a Thorlabs beam profiler, first somewhere just after the expander, and second at the focus of the first lens. The former is used to adjust the beam shape and quality over the widest possible frequency range, and the latter to

compensate powers in each tone. Fig.4.2(a) shows the beam profiles of the diffracted order for a drive spanning 10 MHz about 25 MHz (center frequency – $F_c$). The last of the profiles is of the expanded beam without passing first through an AOD. Visually, there is a clear degradation in quality of the Gaussian beam due to the AOD. Careful adjustment of the entry polarization of the trapping laser as well as pitch/yaw of the AOD needs to be performed to maximize the usable frequency range. Fig.4.2(b) and 4.2(c) shows the AOD Diffraction efficiency spectrum and the power-compensated array of tweezers for 1-tone, 2-tone, 3-tone, 4-tone and 5-tone drive with spacings determined by the previously obtained usable range. Compensation is easily programmable using the AWG, whose 20 DDS cores enable individual digital control over the amplitude, frequency as well as phase offset of each RF tone, necessary to perform uniform trapping of atoms.

### 4.1.3 Trap Frequencies

The harmonic approximation of the trap near the bottom of the potential well results in the restoring gradient force as given in Eq.(2.13). The axial and radial trap frequencies can then be derived from the stiffness constants simply as $f = \frac{1}{2\pi}\sqrt{\frac{k}{m}}$:

$$f_r = \frac{1}{2\pi}\sqrt{\frac{4U_0}{mw_0^2}} \; ; \; f_z = \frac{1}{2\pi}\sqrt{\frac{2U_0}{mz_R^2}} \tag{4.1}$$

Experimentally, the trap frequencies were determined using the following method. First a large number of atoms is loaded into a single trap from the MOT cloud for a few seconds, and then the trap power is modulated by performing amplitude modulation of the RF tone with a low deviation for 100 ms [6].

The experimental sequence for this measurement is provided in Fig.4.3(a). When the modulation frequency matches twice the trap frequency, parametric heating causes a loss in atom numbers, resulting in a dip in fluorescence count. By sweeping the modulation frequency, we obtain the following fluorescence curves ($\propto$ atom retention probability) as shown in Fig.4.3(b).

Two dips corresponding to twice the axial and radial trap frequencies are obtained, thus the measured values are 1.5 kHz and 15 kHz respectively. Hence, from these values, one can back calculate the beam waist and trap depth. The experimentally determined beam waist is 1.83 $\mu$m, while the trap depth is around 80 $\mu$K. The former result agrees well with the preliminary measurement of 1.80 $\mu$m. A few hundred micro-Kelvins deep trap is sufficient to load and sustain single atoms. However, the measured low trap depth can be owed to the high optical loss in the microscope objective and probable under-estimation due to modulation depth inconsistencies across the frequency spectrum.

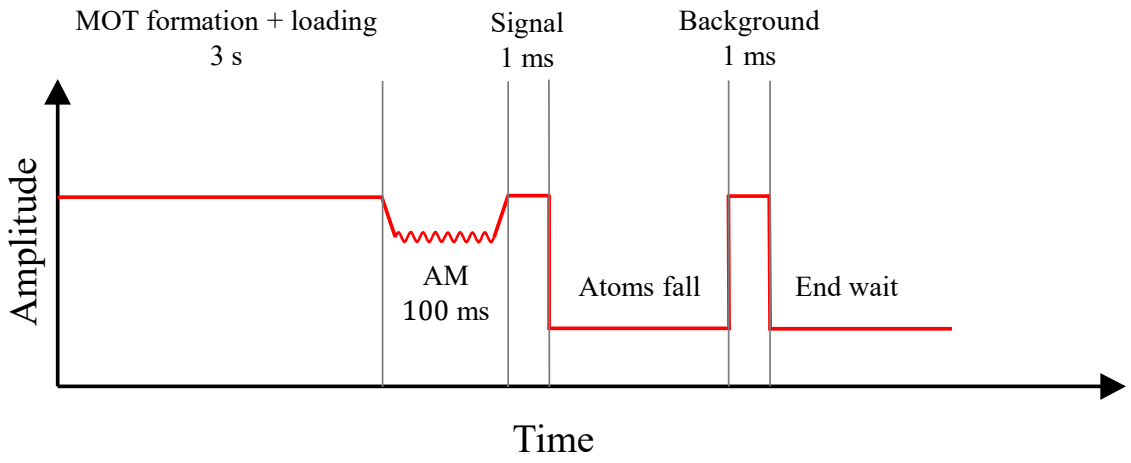


(a)

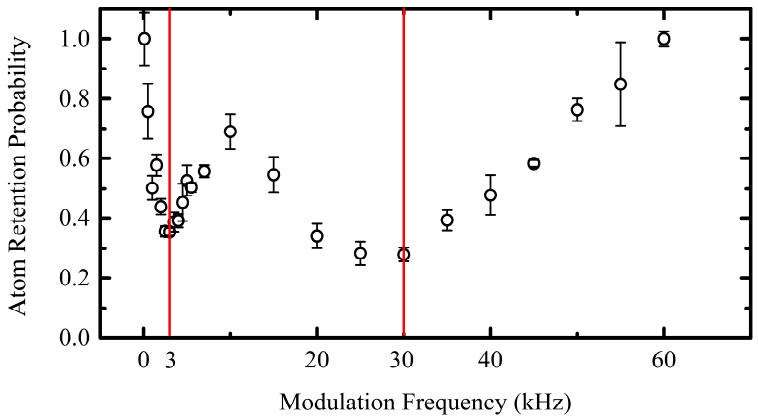


(b)

Figure 4.3: (a) Experimental sequence for the AOD RF amplitude; (b) Measured frequencies are 1.5 kHz and 15 kHz in the axial and radial directions.

### 4.1.4 Temporal response of AOM

As mentioned in Section 2.2.2, AOMs can be used to generate time-shared arrays. Such an array can be generated by rapidly cycling the diffracted order of the trapping light through all the lattice points in the array, such that the trapped atom sees a time-averaged trapping potential that is deep enough to be able to confine it, just like a static tweezer. This allows reconfiguration in 2-D without the necessity for a pick-drop tweezer like in the case of the hybrid SLM-AOD setup. However, for this application, the switching frequency of the AOM must vastly exceed the harmonic trap frequencies multiplied by the number of intended lattice points – $f_s \gg f_r \times N$. With the prior information on measured trap frequencies from the previous section, a temporal response characterization is necessary to check the feasibility of this idea.

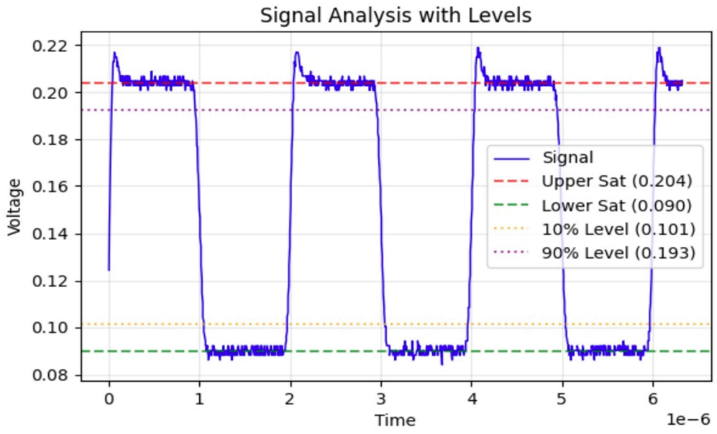


(a)

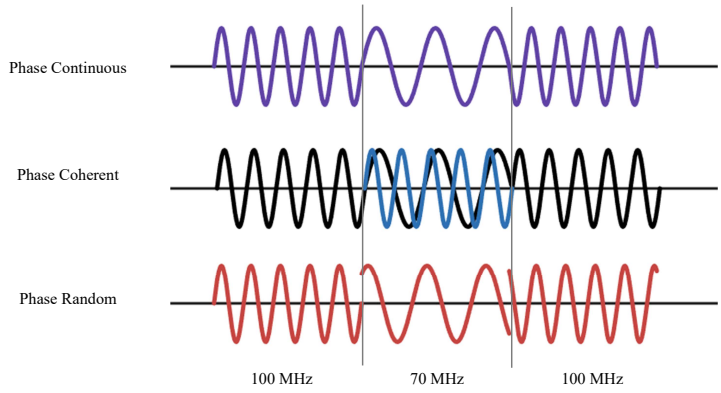


(b)

Figure 4.4: (a) Digital signal obtained from photodiode on an oscilloscope; (b) Phase modes for streaming time-shared tones.

The first diffracted order of a 1 mm beam from an AOM centered at 100 MHz is focused onto a fast photodiode (7 ns) connected to an oscilloscope. The AWG streams a time-shared multi-tone (100

MHz & 70 MHz) with each sinusoidal tone lasting a microsecond. The recorded signal is as shown in Fig.4.4(a). From this, a 90 % − 10 % fall/rise time measurement at the edges can be obtained. Of interest to note is the sensitive dependence of the responsivity on the relative phases of the streamed tones. The various phase streaming modes and the associated responsivity behaviours is summarized in Fig.4.4(b) and Tab.4.1 respectively. We can notice that the phase-continuous mode gives the shortest fall time while the phase-random mode gives the shortest rise time. The slow diffusion of carriers outside the depletion region in a photodiode along with the RC time-constant renders the fall time a non-reliable quantity, hence we can conclude that the phase-random streaming mode achieves the fastest switching rates ($f_s \approx 15.5$ MHz), which surpasses the expected rate of 15 MHz for a $10 \times 10$ array.

| Streaming mode | Rise time (ns) | Fall time (ns) |
|---|---|---|
| Phase continuous streaming | 70.0 | 88.6 |
| Phase coherent streaming | 70.0 | 82.6 |
| Phase random streaming | 65.4 | 90.0 |

Table 4.1: Phase modes effects on temporal responsivity of AOM

## 4.2 Atom Characterisations

### 4.2.1 Atom Loading Trends

After having characterized the tweezers, we now check the loading trends of atoms into the tweezers. A singular tweezer is switched on simultaneously during the MOT formation step lasting few seconds, serving as the loading step. The probe beam with variable detuning (red-/blue-detuned) is switched on for 40 ms towards the end of the loading, which serves to induce the light-assisted collisions. Then, the MOT lights are turned off and the cloud is allowed to fall and diffuse for 1 s, while also ramping down the quadrupole magnetic field to zero. The atom signal is acquired by pulsing the probe cooling and repumper light for a variable amount of time $t_p$ lasting one to few milliseconds, and collecting the atom fluorescence on the EMCCD with an EM gain of 300. A background signal is also taken using a secondary probe pulse after dropping the atoms out of the tweezer. All frequency detunings when the tweezers are switched on take into account the total light shift (AC Stark shift) on the $5^2S_{1/2} \longrightarrow 5^2P_{3/2}$ transition ($\approx 20$ MHz towards the blue side of the bare-atom resonance) due to the highly intense trapping light at the focus. The experimental sequence is visualised neatly in Fig.4.5(a).

As previously seen in Eq.(2.15), the occupation number of a tweezer can be modelled using a second order differential equation involving a loading rate R, a one-body loss co-efficient $\alpha$ owing

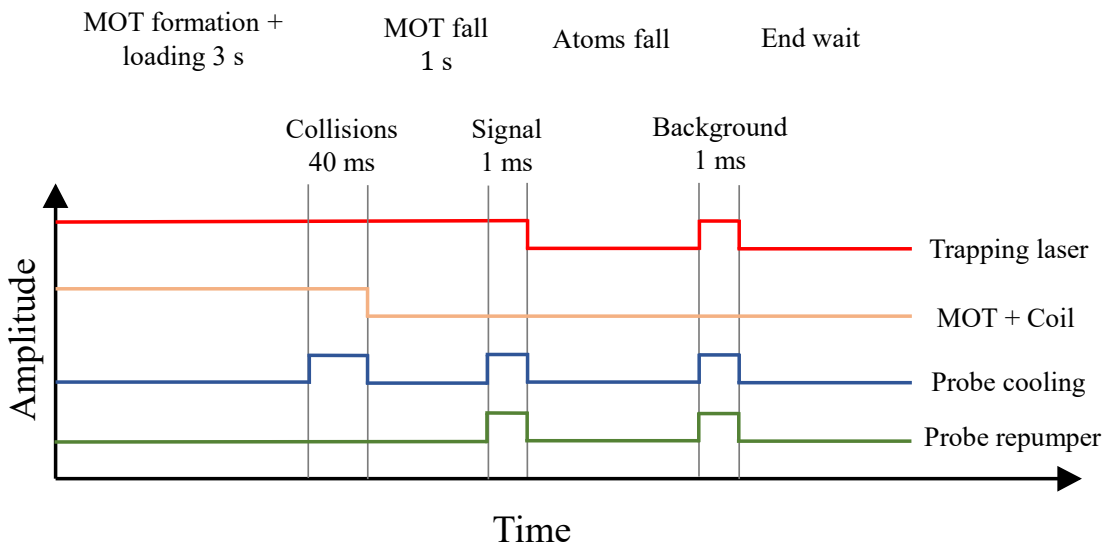


(a)

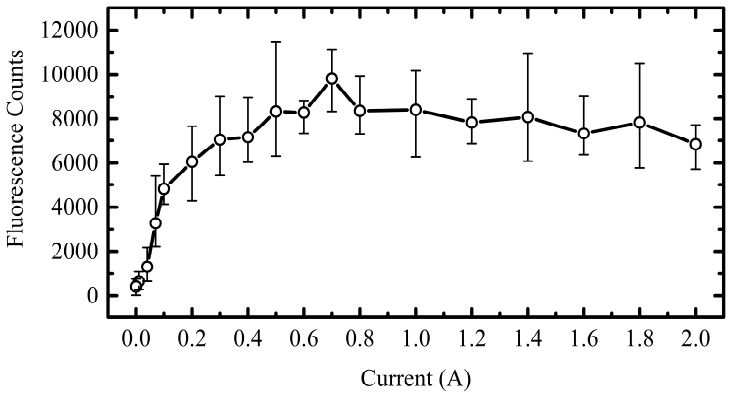


(b)

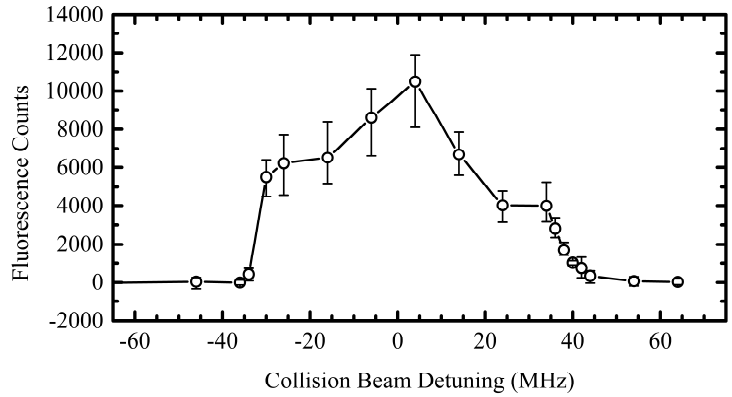


(c)

Figure 4.5: (a) Experimental Sequence; (b) Quadrupole field coil current effect on mean occupation number; (c) Collision beam detuning effect on mean occupation number.

to the background vapour collisions and a two-body collision co-efficient due to the inelastic LACs. Experimentally, we have direct as well as indirect control over $R$ and $\beta$. The loading rate depends on numerous variables such as MOT cloud density, atom temperature, MOT induced collisions, trap volume etc. These are tied to experimental variables such as the quadrupole magnetic field current, oven temperature, Zeeman slower and MOT light detunings. The two-body collision co-efficient depends on the collision beam detuning and power, and is also extremely sensitive to trapping volume ($\beta \propto w_0^{-4}$). Of these, we are interested in checking the fluctuation of mean occupation number $\langle N_{occ} \rangle$ (represented by the expectation value of the fluorescence count) as we vary $R$ controlled via the quad coil current, and $\beta$ controlled via the collision beam detuning. These trends are shown in Fig.4.5(b) and 4.5(c). While taking the measurements with the quad coil current sweep, the probe is kept slightly red-detuned to resonance to avoid LACs deteriorating the fluorescence. From Fig.4.5(b), we clearly see a distinct drop in the average fluorescence counts, as the quad coil current reduces to zero from the standard MOT operational value of 2 A, This can be owed to the reducing MOT cloud density as the magnetic field gradient relaxes [24]. A peak and a slight subsequent decrease somewhere in the intermediate current levels before the plateau at higher values is explained by the increasing field gradient not being able to capture atoms at the higher end of the velocity distribution, thus lowering the phase-space density.

For the measurement of dependency on the collision beam detuning, initially a large enough loading rate is maintained during the collisions process just before letting the MOT fall. This ensures that the loading rate doesn't meddle with the collisions. In Fig.4.5(c) we notice that the mean fluorescence count peaks at a collision beam detuning of around 4 MHz, suggesting weak collisions rate or a very low $\beta$ near resonance. However, the mean fluorescence count, hence the mean occupation number, reduces dramatically to sub-Poissonian values towards the large red ($-34$ MHz) or blue ($+44$ MHz) detuned regime. The fact that the onset is dramatic and short-lived, shown by near zero fluorescence (just background amplified noise) with anymore detuning on both sides, is proof that we might not be inside the robust collisional blockade regime, where at most one atom can exist stably inside the trap. However, light-assisted collisions can still dominate within a very small parameter space, proved by the observed trends in this section. The next section will probe the statistics and the reason for this behaviour.

### 4.2.2 Loading Statistics into a Tweezer

Here, we study the loading statistics of atoms into the current tweezers. We do not expect a robust collisional blockade regime for the measured beam waist of 1.77 $\mu$m, since the trap doesn't meet the criterion of being sub-micron, as established in [25]. However, the traps can be loaded with a sub-critical loading rate $R$ with the collision beam detuned accordingly for a close-to-unity mean

occupation. The MOT cooling and repumper frequency detunings and amplitude; probe imaging, LAC beam and repumper frequency detunings and amplitude; quadrupole field coil current; and pulse durations are carefully dialled while continuously monitoring the fluorescence pattern over time to reach discretisation or bi-/multi-modal behaviour.

For this thesis, we probed both red-detuned as well as blue-detuned collisions as the main single atom loading strategy. The fluorescence datasets upon binning suggest the probabilistic loading of 0, 1, 2 and 3 atoms into the tweezer. The obtained histograms show multi-modal signatures in both red- and blue-detuned collisional regimes, as shown in Fig.4.6(a) and 4.6(b). However, the contrast between the peaks is poor due to high optical losses in the imaging path. A compensatory increase in probe pulse duration is not possible due to increased scatter amplified by the EM gain. Thus, despite the fit, a confident statement on the bi-modality, or even the discretisation of occupation number cannot be made.

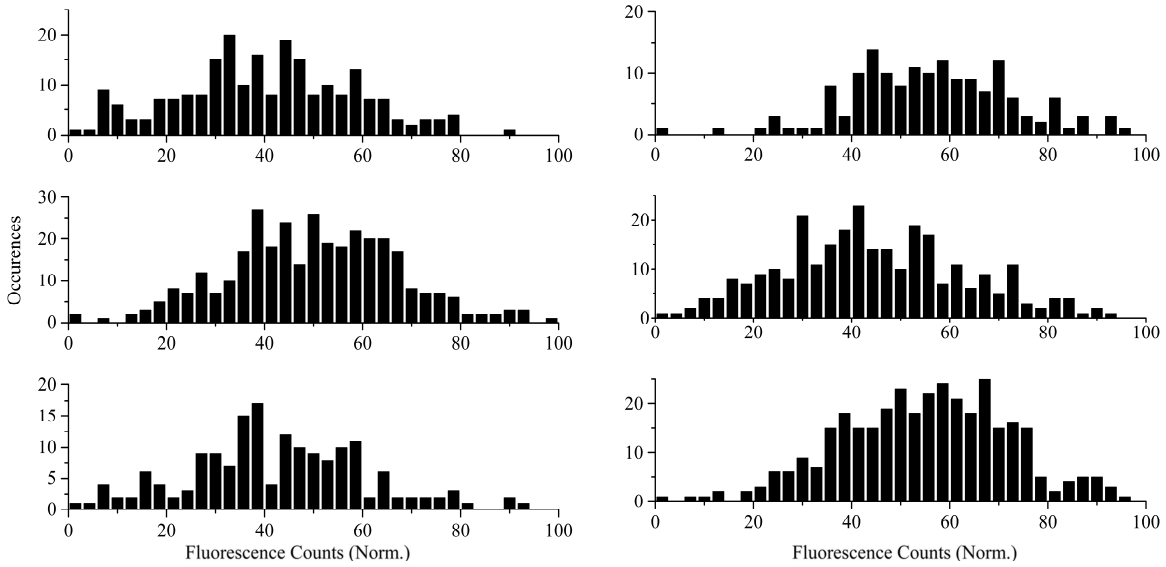


Figure 4.6: (a) Red-detuned collisions; (b) Blue-detuned collisions.

### 4.2.3 Preparation of an Array

An attempt to generate an array in one dimension using the AOD is demonstrated in this section. With the pre-calculated amplitude compensation obtained in Section 4.1.2, we provide 2- and 3-tone RF drives to one of the axes of the AOD. It is observed that a slight heat-out of atoms in the direction of probe beams occur, probably due to the unwanted collisions induced in the imaging process, although the probe and repumper are kept near resonance. This is the reason that the resolution is not good along this axis, hence we provide the multi-tone only along the other axis.

The obtained tweezer arrays are displayed in Fig.4.7(a) and 4.7(b). An array beyond three tones was not possible to generate despite multiple efforts to optimise compensatory amplitudes and minimising optical losses. However, an unmitigable but large optical loss comes from the huge trade-off in transmission factor of the trapping laser wavelength and diffraction efficiency of the first order in exchange for a wide workable frequency range and usable beam profile. This is due to the mismatch between the operational wavelength of 1064 nm of the AOD, and the trapping laser wavelength of 813 nm.

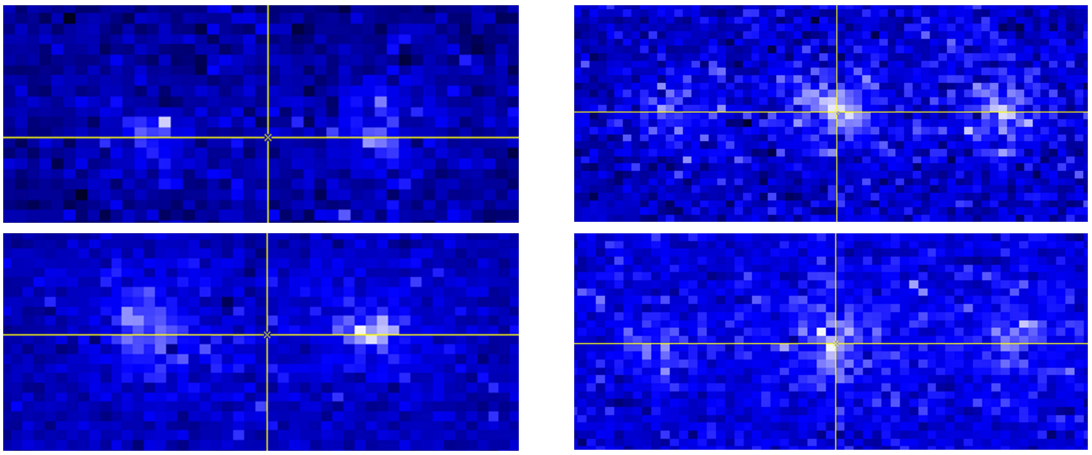

(a) (b)

Figure 4.7: (a) 2-tone array; (b) 3-tone array.

## 4.3 Vacuum Bake-out of the Miniature Platform

The vacuum pump-down and bake-out process creates the necessary Ultra High Vacuum (UHV $\approx 10^{-10}$ mbar) for single neutral atom trapping with high background collisions limited lifetimes. The procedure is as follows:

| **Bake-out Run** | **Pressure sustained (mbar)** |
|---|---|
| 1 | $2 \times 10^{-8}$ |
| 2 | $4 \times 10^{-8}$ |
| 3 | $5 \times 10^{-7}$ |

Table 4.2: Sustained pressures after bake-out runs

The miniature setup is vacuum-sealed by tightening all CF-flanges using UHV-grade copper gaskets, and is connected to a Turbo-Molecular Pump (TMP) via an elbow from the T-valve, which is in turn attached to a backing scroll pump. After an initial pump down to $10^{-2}$ mbar using the backing,

the TMP is started at low currents and eventually at full current and RPM, for about 24 hours. This brings the vacuum down to the UHV level ($\approx 10^{-9} - 10^{-10}$) mbar). Then, the attached ion pump is started at 5000 V. Once these steps are done, the entire system, including the ion pump, the TMP and the elbow is wrapped in Aluminium foil and resistive heating bands. The bake-out is started at about 40 °C and slowly the temperature is increased uniformly over a whole day under constant monitoring to about 120 °C. The Torr Seal application prevents a bake-out over this temperature due to its cracking point. A subsequent short firing of the ion-gauges and getter material releases initial excess vapours and degas the surface contaminants, to be pumped out by the TMP. Later, the system is cooled down to room temperature and the TMP is disconnected, while leaving the ion pump operational at 3000 V.

However, our setup could not sustain UHV due to an inadvertent cracking of the Torr Seal layer during the bake-out process, as well as a leaky T-valve. The sealant application was topped up with a thicker layer for another couple of trials, but the internal degassing of the trapped air pockets can be the explanation for not reaching the necessary UHV level. The vacuum levels reached are summarised in Tab.4.2.

# Chapter 5

# Discussion

## 5.1 Outcomes

To summarise the outcomes so far, the trap was characterised for its beam waist, trap depth and frequencies before performing the atom loading experiments. The obtained beam waist of 1.83 $\mu$m, as also confirmed by the preliminary tests confirms that we are just shy of the collisional blockade regime, in contrast to the higher tolerance of the regime upto 4 $\mu$m reported in [13]. The relatively small numerical aperture of 0.28 provided by the microscope objective is unsatisfactory for obtaining sub-micron beam waists necessary to enter the robust single atom loading regime. Despite the shortcomings, we were able to display near sub-Poissonian loading in a very narrow parameter space, obtainable by a weak loading rate from a rarefied MOT cloud (quadrupole field coil current $\longrightarrow$ 0 A) and operating with the collision beam detunings that provided somewhat $\langle N_{occ} \rangle \approx 1$. A 1-D array of upto 3 tweezers could be demonstrated with the available optics and opto-electronics.

The attempt at a miniature assembly did not fare well due to the inadequate engineering of the vacuum glass chamber, which could not deliver a sustained UHV post bake-out. However, this compact version reduces the unwanted optics and over-engineered parts that is visible on the current Rb BEC setup for a single atom trapping experiment.

The trap frequency measurement and subsequent AOM temporal characterisation provided a promising confirmation for the generation of time-shared tweezer arrays. With a nearly 15 MHz switching rate, $N \times N$ arrays upto $N = 10$ can be obtained.

## 5.2 Future Outlook

The deep insights gained from our experiments is advantageous in the planning for the next generation of single neutral atom trapping efforts, as will be outlined below.

The certain assertion that only a sub-micron beam waist can deliver the necessary collisional blockade regime for single atom loading motivates the use of a higher numerical aperture objective lens ($NA = 0.55$), whose working distance of 15 mm is compatible with a newly ordered custom vacuum chamber for the miniature setup. A new 2-axis AOD suitable for use at 813 nm enables loss-less and high efficiency transmission of the tweezer light. Along with this, the validity checks on the AOM's capability to deliver high speed switching has brought in sights the future plans for implementation of a reconfigurable hybrid SLM-AOD architecture as well as time-shared arrays.

Thus, the future outlook of the trapped single atom arrays is summarised by the implementations mentioned above on the miniature setup. This will help in the long-run motive to develop portable and field-deployable quantum processors based on neutral atoms for quantum computers.

# Bibliography


[1] P. A. M. Dirac, *The principles of quantum mechanics*, Fourth Edition, International Series of Monographs on Physics (Oxford University Press, Oxford, New York, Jan. 7, 1981), 328 pp.

[2] R. P. Feynman, "Simulating physics with computers", International Journal of Theoretical Physics **21**, 467 (1982).

[3] D. P. DiVincenzo, "The physical implementation of quantum computation", Fortschritte der Physik **48**, 771 (2000).

[4] D. A. Steck, *Rubidium 87 d line data*, Los Alamos National Laboratory, Los Alamos, NM 87545, Sept. 25, 2001.

[5] J. Preskill, *Why i called it 'quantum supremacy'*, Quanta Magazine, (Oct. 2, 2019) https://www.quantamagazine.org/john-preskill-explains-quantum-supremacy-20191002/ (visited on 01/31/2026).

[6] H. J. Levine, "Quantum information processing and quantum simulation with programmable rydberg atom arrays", PhD thesis (July 12, 2021).

[7] K. Wintersperger, F. Dommert, T. Ehmer, A. Hoursanov, J. Klepsch, W. Mauerer, G. Reuber, T. Strohm, M. Yin, and S. Luber, "Neutral atom quantum computing hardware: performance and end-user perspective", EPJ Quantum Technology **10**, 32 (2023).

[8] A. Ashkin, "Acceleration and trapping of particles by radiation pressure", Physical Review Letters **24**, 156 (1970).

[9] A. Ashkin, J. M. Dziedzic, J. E. Bjorkholm, and S. Chu, "Observation of a single-beam gradient force optical trap for dielectric particles", Optics Letters **11**, 288 (1986).

[10] S. Chu, J. E. Bjorkholm, A. Ashkin, and A. Cable, "Experimental observation of optically trapped atoms", Physical Review Letters **57**, 314 (1986).

[11] R. Grimm, M. Weidemüller, and Y. B. Ovchinnikov, in *Advances in atomic, molecular, and optical physics*, Vol. 42 (Elsevier, Jan. 1, 2000), pp. 95–170.

[12] V. Lal, "Compact 2d-MOT and 3d-MOT systems for portable quantum gravimeter and quantum simulator", Accepted: 2023-05-19T05:26:00Z, Thesis (May 2023).

[13] N. Schlosser, G. Reymond, I. Protsenko, and P. Grangier, "Sub-poissonian loading of single atoms in a microscopic dipole trap", Nature **411**, 1024 (2001).

[14] M. F. Andersen, "Optical tweezers for a bottom-up assembly of few-atom systems", Advances in Physics: X **7**, _eprint: https://doi.org/10.1080/23746149.2022.2064231, 2064231 (2022).

[15] M. Endres, H. Bernien, A. Keesling, H. Levine, E. R. Anschuetz, A. Krajenbrink, C. Senko, V. Vuletic, M. Greiner, and M. D. Lukin, "Atom-by-atom assembly of defect-free one-dimensional cold atom arrays", Science **354**, 1024 (2016).

[16] F. Nogrette, H. Labuhn, S. Ravets, D. Barredo, L. Béguin, A. Vernier, T. Lahaye, and A. Browaeys, "Single-atom trapping in holographic 2d arrays of microtraps with arbitrary geometries", Physical Review X **4**, 021034 (2014).

[17] M. J. Gibbons, C. D. Hamley, C.-Y. Shih, and M. S. Chapman, "Nondestructive fluorescent state detection of single neutral atom qubits", Physical Review Letters **106**, 133002 (2011).

[18] L. Chen, W.-Y. Zhu, Z.-J. Chen, Z.-B. Wang, Y.-D. Hu, Q.-X. Jie, G.-C. Guo, and C.-L. Zou, "Optimized readout strategies for neutral-atom quantum processors", Physical Review A **112**, 022606 (2025).

[19] Y. H. Fung, A. V. Carpentier, P. Sompet, and M. Andersen, "Two-atom collisions and the loading of atoms in microtraps", Entropy **16**, 582 (2014).

[20] Y. H. Fung, P. Sompet, and M. F. Andersen, "Single atoms preparation using light-assisted collisions", Technologies **4**, 4 (2016).

[21] M. Schulz, "Tightly confined atoms in optical dipole traps", Thesis (Quantum Optics and Spectroscopy, Universität Innsbruck, Innsbruck, 2002).

[22] S. Sarkar, "Ultracold atoms in 1-d optical lattices: experiments towards quantum chaos and atom interferometry", Accepted: 2019-04-16T09:43:40Z, Thesis (Dept. of Physics, Apr. 2019).

[23] S. Kumar, "Towards distributed quantum information processing using coupling of neutral atoms to plasmonic nanostructures", Accepted: 2018-04-24T11:07:02Z, Thesis (Dept. of Physics, Apr. 2017).

[24] S. P. Ram, S. R. Mishra, S. K. Tiwari, and H. S. Rawat, "Temperature and phase-space density of a cold atom cloud in a quadrupole magnetic trap", Journal of the Korean Physical Society **65**, 462 (2014).

[25] N. Schlosser, "Collisional blockade in microscopic optical dipole traps", Physical Review Letters **89**, 10.1103/PhysRevLett.89.023005 (2002).